國立臺灣大學理學院物理學系
碩士論文
Department of Physics
College of Science
National Taiwan University
Master Thesis

基於相對論性雷射電漿飛鏡之模擬黑洞研究
Analog Black Hole Based on Relativistic Laser-Plasma
Flying Mirror

劉詠鯤
Yung-Kun Liu

指導教授：陳丕燊博士
Advisor: Pisin Chen, Ph.D.

中華民國 109 年 6 月
June, 2020

誌謝

三年的碩士生涯，即將到了尾聲。對於未來要繼續在學術這方向上前進的決定，除了期待還有點擔心，不太確定自己的能力是否能在這條路上立足。回想在碩士班研究期間，也是遇到許多迷茫與挫折，但也受到了許多人的幫助與鼓勵。希望藉此機會回顧，期許自己不會忘記這些時光以及各種收穫，也作為將來繼續邁進的養分。

首先，很感謝我的指導教授陳丕燊老師。老師深具啟發性的指導，讓我了解到物理學不同領域之間，並非是獨立無關的。透過深入研究不同領域，往往可以找到互相借鑑、啟發的想法，甚至能夠做出重大的突破。例如我碩士期間所參與的類比黑洞計畫，即為結合雷射電漿以及宇宙學所提出的跨領域構想。這也提醒我在未來的學術生涯中，要時時保持對各領域的好奇以及勇於發想創意的熱情。感謝口試委員裴思達老師以及汪治平老師在組會以及口試時對於論文以及研究方向提出的意見。尤其是汪治平老師，總是會以實驗學家的嚴謹精神，督促我仔細考慮清楚每一個細節。使我不會得過且過，能夠盡量將每個環節想清楚，這過程往往可以成為更進一步研究的穩固基石。陳老師的敏捷熱情與汪老師的謹慎細緻，都是我未來努力的目標。此外，也很感謝幫我撰寫博士班推薦信的趙挺偉老師、薛熙于老師，在兩位老師的數值物理相關課程中，學習到了非常多的數值計算知識，對於進入模擬領域，有非常大的幫助。

此外，特別感謝研究室的博士後方遠學長。感謝學長不厭其煩的和我討論未來的研究方向、如何改進研究成果、如何撰寫期刊論文等等。如果沒有學長的幫忙，我碩士研究期間應該會走非常多的彎路、面對迷茫而不知所措。感謝在捷克的合作對象，Petr Valenta 對於我在模擬上提供了非常多的

建議，期待我們能繼續合作。感謝中央大學的劉耀灃學長，引導我走進了 PIC 模擬的大門。

此外，感謝 LeCosPA 的所有成員們，一起 meeting、茶會、期刊讀書會等等活動，從大家身上學到許多東西。感謝 AnaBHEL 組內的學弟妹們，至恩、冠男教了我許多場論、理論相關內容。和爲寧、冠宏討論模擬、理論相關問題時，激盪出了不少的想法。特別感謝秘書們，幫我們安排會議時間表、處理各種行政事務，以及最重要的: 帶我們出去聚餐!

感謝我的朋友們，家恩、育翔、中鳴、健庭、能賢、宇霆、芸瑄等等。研究碰到阻礙時，很幸運有你們可以一起聊天、走走，不同的生活、背景總能使我走出自己的小圈圈，使我重新以不同角度思考問題。也謝謝系羽的大家，孟哲學長、邦漢、聖義，努力地找我去打球，爲我的生活注入更多活力。也感謝在口試前一段時間，進入我生活圈的靜文，一起聊天、散步，爲我分散了非常多準備口試、趕論文的焦慮。

特別感謝我的家人們，爸爸媽媽對於我不走尋常路、追求理想的無條件支持，使我能夠十分放心的做自己想做的事。爸爸持續讀法律書充實自己、媽媽工作之餘參與編撰教科書以及哥哥同時準備司法官考試以及碩士的強大毅力，家人們身體力行的精進，給予我很大的鼓勵與鞭策。住在台北的秋味姑姑時常美食、水果、點心支援，是我生活中堅強的後勤部隊。十分感謝我的家人對我的全方位支持與幫助，沒有你們，就沒有今天的我。

最後，有太多太多的人需要感謝，感謝你們的鼓勵、提醒、刺激。謹以此論文獻給諸位!

摘要

　　自 1974 年霍金提出黑洞蒸發理論後，關於霍金輻射是否導致資訊遺失的爭議，持續吸引理論物理界之興趣。但由於宇宙中自然存在的黑洞放出之霍金輻射過於微弱，超出了目前所具備的觀測能力。為了更深入研究此問題，以及和理論預測互相驗證，在實驗室中產生「類比黑洞」的設計被陸續提出。其中一種模擬黑洞模型：飛鏡模型（Flying Mirror Model）描述一在閔考斯基空間具有特定移動軌跡的邊界，可以用來類比彎曲空間附近的物理。基於此飛鏡模型以及強場雷射在電漿中產生相對論性電子飛鏡的現象，Chen and Mourou 於 2017 年提出了「桌上型類比黑洞實驗」(Analog Black Hole via Lasers, AnaBHEL) 之構想。

　　本論文研究內容，主要集中於此雷射電漿飛鏡之性質，例如：此飛鏡之反射率、入射雷射及飛鏡交互作用後之反射頻譜以及如何透過改變背景電漿密度控制飛鏡軌跡等等問題。透過數值模擬及電漿理論模型，我們對於雷射電漿飛鏡進行深入的分析研究，能提供 AnaBHEL 實驗更多必要資訊。

　　在第一章中簡單回顧了霍金輻射及資訊遺失悖論的議題，以及類比黑洞的概念。我們主要介紹了類比黑洞的飛鏡模型，不同的飛鏡軌跡，會釋放出不同的能量通量 (Energy Flux) 及頻譜。此外介紹了在研究雷射電漿交互作用使用的模擬工具、理論。模擬部分，我們介紹了粒子網格模擬 (Particle In Cell Simulation) 中用到的概念及重要的演算法。理論部分，回顧了在雷射電漿交互作用領域中用到的基本概念。

　　第二章我們討論了背景電漿密度是如何影響相對論性飛鏡之速度。飛鏡速度除了在類比黑洞實驗中扮演重要的角色外，也在雷射尾場粒子加速器中有著重要的影響。我們首先介紹了雷射在電漿中產生非線性尾隨場的理論。

之後，我們利用此理論，對於飛鏡和驅動光的距離進行理論討論。再來介紹了在梯度電漿密度背景下，計算飛鏡速度之兩種方法。在以往文獻中，第一面相對論性飛鏡被認爲和驅動雷射相距一個電漿波長，但我們透過理論研究發現，此距離和電漿波長實際相差一個係數。若無考慮此係數的修正，以上兩種估算飛鏡速度的方法，皆會高估速度的改變量。

第三章我們討論了相對論性飛鏡的反射率問題。相對論性飛鏡爲一層密度極高的電子組成，其反射率可以透過估計此電子層密度分布以及解一入射電磁波在此電子層上的邊界條件、波動方程式來進行計算。我們首先回顧了過往對於此問題的研究，在將過往研究結果和我們執行的一維模擬比較時，我們發現在特定的情況下，以往之電子密度模型對反射率有高估的現象。因此我們根據模擬中的電子分布，提出不同的擬合模型，並獲得和模擬數據吻合的結果。此外，以往研究集中討論於一相對論飛鏡及平面波的交互作用。本章後半，我們將此理論延伸至具有有限脈寬的入射波 (以高斯分布爲例)，發現有限脈寬入射波的反射頻譜，其峰值會和平面波結果具有一定偏移。

關鍵字： 類比黑洞、粒子網格模擬、雷射電漿交互作用、相對論性飛鏡、雷射電漿尾隨場

Abstract

Since Hawking proposed the theory of black hold evaporation in 1974, the debate that whether Hawking radiation causes information loss attracts theoretical physicists. One way to set down the debate is through direct observation. However, the Hawking radiation emitted by astrophysical black holes is too weak to be observed due to the large mass of black hole. To dig into this issue and verify the theoretical predictions, several schemes of "Analog Black Hole" had been proposed to observe the black hole radiation in the Lab. One of these Analog Black Hole models, the flying mirror model, describes that a boundary with specific trajectory in Minkowski space can mimic the physics around curved-spacetime. On the basis of this model and the phenomenon that an intense laser can generate a relativistic flying mirror in plasma, Chen and Mourou proposed the experiment "Analog Black Hole via Lasers, AnaBHEL".

This thesis mainly focuses on properties of laser-driven flying plasma mirror, such as the reflectivity, the reflected spectrum as an incident laser pulse interacts with the mirror and the relation between the trajectory of the flying mirror and the background plasma density. These studies are based on numerical simulations and cold collision-less plasma theory. These studies can provide essential information for the AnaBHEL experiment.

In chapter 1, we briefly review the issue about Hawking radiation, information loss paradox and proposals about analog black hole. In the flying mirror model, different trajectories of the flying mirror emit different energy

flux and frequency spectrum. Besides, we introduce the simulation tool and the theory to study laser plasma interaction. In simulation part, we explain the concept and algorithm of Particle In Cell simulation. In theory part, we review the basic plasma theory and the interaction between laser and plasmas.

In chapter 2, we describes how the background plasma density affects the velocity of the flying mirror. The velocity of mirror plays an important role in not only analog black hole experiment but also the Laser Wake Field Accelerator (LWFA). We first introduce the one-dimensional nonlinear theory of the laser-driven wakefield and utilize this theory to investigate the distance between driver laser pulse and the flying mirror. Then, we review two methods to calculate the velocity of flying mirror in an inhomogeneous plasma background. In previous literature, the distance between first plasma mirror and the driver is thought to be a plasma wavelength. However, we find the distance differs from plasma wavelength by a coefficient. With this corrected term, the velocity of flying mirror can be calculated more accurately.

In chapter 3, we study the reflectivity of the flying mirror. The relativistic flying plasma mirror is composed with a dense shell of electrons. The reflectivity can be estimated by the density distribution of electrons and solving the wave equations with proper boundary condition of an incident wave. First, we review previous studies on this problem. We found previous model of the electron distribution seems to overestimate the reflectivity compared to 1D simulation results. Therefore, we proposed a density distribution fitting model and get results which agree well with simulation data. Besides, previous study mainly discussed the interaction between the flying mirror and a plane incident wave. In the second half of this chapter, we extend the study to a finite bandwidth incident wave (the Gaussian profile is considered). We find a deviation of the peak frequency of reflected spectrum exists compared to the result of a plane wave.

Interaction, Relativistic Flying Mirror, Laser Driven Wakefield

x

Contents

List of Figures

List of Tables

Chapter 1

Introduction

1.1 Analog Black Hole and Moving Mirror Model

Black holes are sites with enormous gravity. In classical theory, the gravitation of black hole is so huge that nothing, not even photon can escape from this gravitational singularity. However, in 1974, within the framework of quantum field theory in curved spacetime, Stephen Hawking discovered that the quantum effect allows black hole to emit black body radiation [2], the so-called Hawking radiation. The Hawking radiation reduces the mass and angular momentum of the black hole, therefore leads to the "black hole evaporation". Such process may result in the loss of information [3]. Conservation of information, or probability, in a physical process is a fundamental basis of quantum mechanics and quantum field theory. The possibility that black hole evaporation may result in the loss of information therefore implies a conflict between general relativity and quantum theory, the two fundamental pillars of modern physics. There have been proposed solutions and endless debates about this paradox over the past 40 years, but are essentially all theoretical (see [4] for more details). The difficulties to observe black hole evaporation in our universe is due to the gentle evaporating rate. Without absorbing extra energy, a solar mass black hole will evaporate over 10^{64} years which is apparently longer than the life of the universe. Accordingly, to conquer the information loss paradox, ideas of analog black hole are resorted. Unruh proposed the idea of acoustic black hole [5] to construct the horizon in the fluid system. Based on this scheme, analog black hole based on Bose-

1

Einstein condensate [6, 7, 8] and Superconducting Quantum Interface Device (SQUID) [9] are all demonstrated. On the other hand, it has been long recognized that a time-dependent Dirichlet boundary condition in 1+1D Minkowski spacetime is possible to generate particles out of the initial vacuum state [10, 11, 12]. The particle generation origins from the interaction between a moving boundary and the vacuum fluctuation of the quantized fields, therefore these phenomena are termed the names:"Dynamical Casimir Effect" or "Moving Mirror Model". The analogy between black hole evaporation and moving mirror model had been investigated in [13]. Based on this analogy, the idea of Analog Black Hole Evaporation via Lasers (AnaBHEL) [14] was proposed in 2017.

1.1.1   1+1D Moving Mirror Model

The moving mirror model in 1+1D can be described by a quantized massless scalar field $\psi(t, x)$ in flat spacetime subjects to the Dirichlet boundary condition, $\psi(x = z(t), t) = 0$, where $z(t)$ is the trajectory of the mirror. This boundary condition forces the field to disappear on the boundary therefore describes a perfectly reflecting mirror. The scalar field satisfies the Klein-Gordon equation,

$$\Box\psi = (-\partial_t^2 + \partial_x^2)\psi = 0. \tag{1.1}$$

The inner product of any two solutions of Eq.(1.1) is defined by,

$$(\phi_1, \phi_2) = -i \int_\Sigma d\Sigma^\mu [\phi_1 \overleftrightarrow{\partial_\mu} \phi_2^*] = -i \int_\Sigma d\Sigma^\mu [\phi_1 \partial_\mu \phi_2^* - \phi_2^* \partial_\mu \phi_1], \tag{1.2}$$

where Σ is a Cauchy surface and $d\Sigma^\mu$ is the unit-vector orthogonal to that surface. The orthogonal basis of the solutions can be constructed with Eq.(1.2), which obeys

$$(u_i, u_j) = \delta_{ij}, \quad (u_i^*, u_j^*) = -\delta_{ij}, \quad (u_i, u_j^*) = 0. \tag{1.3}$$

2

After expanding the field operator with a given basis, the creation and annihilation operators $a_i^\dagger, a_i$ are obtained,

$$\phi(x) = \sum_i [a_i u_i(x) + a_i^\dagger u_i^*(x)].\qquad(1.4)$$

The concept of particles is defined based on $a_i^\dagger, a_i$, for example, the vacuum state is constructed by $a_i |0\rangle = 0$.

In 1+1D moving mirror model, it is convenient to move $x - t$ coordinate to the $u - v$ null coordinate defined with $u = t - x$ and $v = t + x$ because the massless modes are all null. Let us consider the condition without a moving mirror, the right-moving modes with positive and negative frequency are

$$\phi_{\omega u} = \frac{1}{\sqrt{4\pi\omega}} e^{-i\omega u}, \quad \phi_{\omega u}^* = \frac{1}{\sqrt{4\pi\omega}} e^{i\omega u},\qquad(1.5)$$

respectively. The left-moving modes are,

$$\phi_{\omega v} = \frac{1}{\sqrt{4\pi\omega}} e^{-i\omega v}, \quad \phi_{\omega v}^* = \frac{1}{\sqrt{4\pi\omega}} e^{i\omega v}.\qquad(1.6)$$

These modes form a set of basis to represent the scalar field in the whole spacetime and the expansion is unique. However, if the moving mirror exists, two different sets of mode, ϕ_ω and $\chi_{\omega'}$ must be used to decompose the field due to the condition introduced by the mirror. In the literature, ω and ω' may be used to distinguish the different set of modes. This leads to different definitions of creation and annihilation operators and therefore different definitions of particle states. The transformation between different modes is the "Bogoliubov transformation",

$$\phi_\omega = \int_0^\infty d\omega' [\alpha_{\omega'\omega}^* \chi_{\omega'} - \beta_{\omega'\omega} \chi_{\omega'}^*],\qquad(1.7)$$

$$\chi_{\omega'} = \int_0^\infty d\omega [\alpha_{\omega'\omega} \phi_\omega + \beta_{\omega'\omega} \phi_\omega^*],\qquad(1.8)$$

3

where $\alpha_{\omega'\omega}$ and $\beta_{\omega'\omega}$ are the Bogoliubov coefficients that can be evaluated as

$$\alpha_{\omega'\omega} = (\chi_{\omega'}, \phi_\omega), \tag{1.9}$$

$$\beta_{\omega'\omega} = -(\chi_{\omega'}, \phi_\omega^*). \tag{1.10}$$
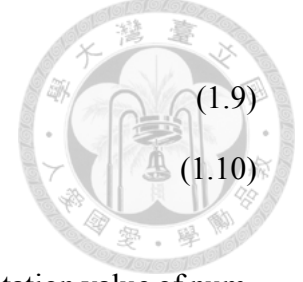
To see the physical meaning of the Bogoliubov coefficients, the expectation value of number operator $N_\omega = a_\omega^\dagger a_\omega$ in the vacuum of $\chi_{\omega'}$ is

$$\langle 0_{\chi_{\omega'}} | N_\omega | 0_{\chi_{\omega'}} \rangle = \int_0^\infty d\omega' |\beta_{\omega'\omega}|^2. \tag{1.11}$$

Therefore, non-zero $\beta_{\omega'\omega}$ implies that the vacuum state defined by the two mode functions are different. The vacuum state for the first mode function is not vacuum for the second one but particles exist. This is an important result in quantum field theory in curved spacetime : vacuum state may not be universally unique.

Consider a perfectly reflecting moving mirror with timelike trajectory $z(t)$, the solutions of Eq.(1.1) are,

$$\phi_{in,\omega'} = \frac{1}{\sqrt{4\pi\omega'}}[e^{-i\omega'v} - e^{-i\omega'p(u)}], \tag{1.12}$$

$$= \frac{1}{\sqrt{4\pi\omega}}[e^{-i\omega f(v)} - e^{-i\omega u}], \tag{1.13}$$

where $p(u)$ and $f(v)$ are called "ray tracing functions" which guarantee the mode functions to vanish on the mirror,

$$p(u) = 2t_u - u, \qquad u = t_u - z(t_u) \tag{1.14}$$

$$f(v) = 2t_v - v, \qquad v = t_v + z(t_v). \tag{1.15}$$

The terms t_v and t_u can be understood as the time coordinate when the null rays and the mirror intersect. For a non-asymptotically null mirror, the general expression of $\beta_{\omega'\omega}$ can

4

be derived [15],

$$\beta_{\omega'\omega} = \frac{1}{4\pi\sqrt{\omega'\omega}} \int_{-\infty}^{\infty} dv(\omega' - \omega f'(v))e^{i\omega'v+i\omega f(v)} \tag{1.16}$$

$$= \frac{1}{4\pi\sqrt{\omega'\omega}} \int_{-\infty}^{\infty} du(\omega'p'(u) - \omega)e^{i\omega u+i\omega'p(u)}. \tag{1.17}$$

Generally speaking, the particle spectrum of any trajectory of mirror can be calculated with the Bogoliubov coefficients. However, the analytical form of ray-tracing functions are difficult to obtain for arbitrary trajectories. Therefore, the analytical result only exists in quite limited case (see summary in [15]). Here, we briefly introduce two different famous trajectories which emit thermal radiation: the modified Davies-Fulling (DF) and Carlitz-Willey (CW) trajectories.

The most famous moving mirror trajectory is DF trajectory [16] because it was the first trajectory proposed to understand the appearance of a thermal spectrum. However, the original calculation utilizes some subtle approximations such that Fulling concluded that although the final results still hold, the approach may have an error [17]. In [15], the author suggested a "late time Davies-Fulling" trajectory which can prevent obscure approximations.

$$z(t) = \begin{cases} -t - Ae^{-2\kappa t} + B & t \to \infty, \\ 0 & t < 0, \end{cases} \tag{1.18}$$

where A, B are some constants and κ characterizes the acceleration of the mirror. The velocity of the mirror is 0 initially and approaches -1 in the future infinity ($t \to \infty$). The Bogoliubov coefficient is,

$$|\beta_{\omega'\omega}|^2 \approx \frac{1}{2\pi\kappa\omega'} \frac{1}{e^{2\pi\omega/\kappa-1}} \quad \text{for } \omega' \gg \omega, t \to \infty, \tag{1.19}$$

which describes a late-time thermal emission in the high frequency limit, $\omega' \gg \omega$.

On the other hand, the CW trajectory [18] gives all-time thermal spectrum and constant

5

energy flux. The trajectory written in the form of $z(t)$ is found in [15],

$$z(t) = -t - \frac{1}{\kappa} W(e^{-2\kappa t}),$$

(1.20)

where W is the Lambert W function (product logarithm) and $\kappa > 0$ is a characteristic parameter about the mirror acceleration. The Bogoliubov coefficient is

$$|\beta_{\omega'\omega}|^2 = \frac{1}{2\pi\kappa\omega'} \frac{1}{e^{2\pi\omega/\kappa-1}},$$

(1.21)

which is a thermal spectrum in 1+1D. The corresponded temperature of CW trajectory, $k_B T = \kappa/2\pi$, is constant for all time, therefore may be an analogy to an "Eternal Black Hole".

The correspondence between trajectories and the emitted particle spectrum provides a way to investigate the evolution of black hole. Accordingly, different trajectories may mimic different candidates of the end stage of black hole [19]. In 2017, Pisin Chen and Gerard Mourou proposed a novel experimental concept using ultra-intense lasers to induce flying mirrors in plasmas with graded density [20]. With a tailored plasma density, different trajectories can be fulfilled [21] and provide a way to investigate different evolution of black hole. The relation between plasma density profile and the mirror trajectory will be discussed with more details in Sec.2.

1.2 Plasma

The term "Plasma" is first introduced by Langmuir in 1928 [22] to describe the ionized gas near the electrode and usually called the "fourth fundamental state of matter". The plasma consists of a gas of ions and free electrons. Unlike usual gas that is an insulator, the conductivity of the plasma can be treated as infinity due to the free electrons. Typically, the plasma only exists in vacuum. Otherwise, the surrounding air will cool down the plasma such that free ions and electrons will recombine into neutral atoms. Therefore, on the earth, plasma state is rare near ground due to the atmosphere. Only when high energy

6

source exists, the plasma state can maintain, such as the gas near lightning or in ionosphere where high energy cosmic rays intensely collide with the air molecular. On the other hand, plasma state is common in the universe, such as the stellar interiors, gaseous nebulas and the most part of galaxies.
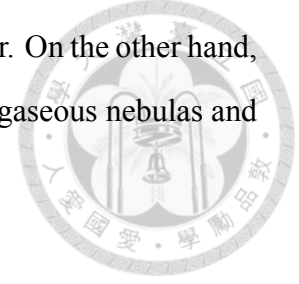
The plasma can be defined as follows [23]:

"A plasma is a quasineutral gas of charged and neutral particles which exhibits collective behavior."

The "quasineutral" property describes the characteristic length scale of the plasma system. A fundamental property of the plasma is the ability to shield the electric potential applied on it. The shielding length is described by the Debye length $\lambda_D = \sqrt{k_B T / 4\pi n_0 e^2}$, where k_B is the Boltzmann constant, T, e and n_0 are temperature, charge and the number density of electrons, respectively. Therefore, for the system with scale L much larger than λ_D, the plasma can be considered as "neutral". The second property "collective" implies that the plasma oscillation frequency $\omega_p = \sqrt{n_0 e^2 / m_e \epsilon_0}$ is much larger than the collision frequency between electrons and neutral particles. This means the electrostatic effect dominates over the gas kinetics of neutral gas.

1.3 Laser Plasma Interaction

After Einstein investigated the relation between the stimulated and the spontaneous emission, people were considering a new way to amplify the electromagnetic field using this phenomenon. Tens of years later, the first working optical laser was finally invented by Maiman in 1960 [24] using the Ruby crystal as the gain medium. After that, this intense and coherent light source got success in quite diverse field, such as military and industry, not to mention the scientific research. In the past tens of years, new techniques to deliver high power and short pulse or extend available wavelength had been developed. Among these progress, we mainly focus on the blooming of the ultra-short pulse laser, which usually refers to the laser with pulse duration from pico-second (ps, $10^{-12}s$) to femto-second (fs, 10^{-15}). In Fig.(1.1), the progress of peak intensity of the laser since 1960 is shown. The increase of the intensity reaches a plateau in around 1970. At that time people can not

amplify the light pulse further without damaging the laser gain medium. The invention of Chirped Pulse Amplification (CPA) [25] conquered this dilemma and opened a new era of ultra-short high intensity laser. Thanks to this technique, the laser peak intensity is still growing nowadays. Due to the short interaction time between the laser and the material, the ultra-short-pulse laser is widely used in material processing, cornea surgeries, molecular interaction, and so on. Among these applications, the one relevant to this thesis is the Laser Wakefield Accelerator [26]. When an intense laser propagates in the plasma, a wake field (longitudinal electric field) will be generated. The wake field can realize an accelerating gradient ($\sim 100\,GV/m$) [27] that is much larger than the conventional radio-frequency accelerator ($\sim 100\,MV/m$). This provides a promising way to construct next-generation accelerator for pursuing higher particle energies or more compact facilities.
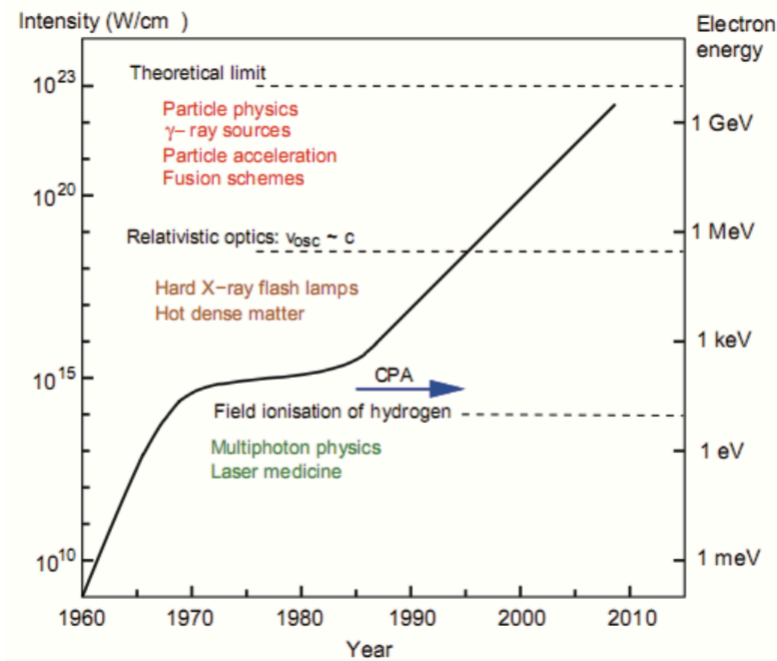
Figure 1.1: Progress of peak laser intensity since 1960 [1].

The intensity of laser can be linked to a Lorentz invariant dimensionless "laser strength parameter", $a_0 = eE_0/m_e\omega c$, where E_0 and ω are the electric field and angular frequency of the laser, with the relation

$$a_0 = 0.85\lambda[\mu m]\sqrt{I[10^{18}Wcm^{-2}]},\qquad(1.22)$$

8

where λ, I are the wavelength and intensity of the laser. For $a_0 \geq 1$, the laser is called "relativistic laser" or referred to as in the "nonlinear regime". Roughly speaking, this terminology can be understood as follows. eE_0/m_e is the acceleration of electrons in electric field and $1/\omega$ is roughly the order of a laser period. Therefore, $eE_0/m_e\omega$ stands for the velocity that electrons can be accelerated in a laser period. Accordingly, $a_0 \geq 1$ implies the electric field can accelerate electrons to near speed of light during one laser cycle, therefore relativistic effect should be taken into account. The intensity of the state-of-the-art $800nm$ Ti:Sapphire laser can achieve $10^{23}Wcm^{-2}$ [28], which corresponds to $a_0 \sim 70$. This highly intense laser provides extreme light pressure within a very short time scale and acquires wide applications in the frontier scientific research (see review [29] for more discussions).

The interaction of ultra-short-pulse laser and matter can be studied from a simple case: the interaction between a single electron and planar electromagnetic field. The motion of electrons can be described by the Lorentz equation,

$$\frac{d\mathbf{p}}{dt} = -e\left(\mathbf{E} + \frac{\mathbf{v} \times \mathbf{B}}{c}\right), \tag{1.23}$$

where $\mathbf{p} = \gamma m_e c^2$ is the momentum and $\gamma = \sqrt{1 + p^2/m_e^2 c^2}$ is the Lorentz factor associated with the electron. The evolution of electron energy follows

$$\frac{d}{dt}(\gamma m_e c^2) = -e(\mathbf{v} \cdot \mathbf{E}). \tag{1.24}$$

Note that the magnetic force $\mathbf{v} \times \mathbf{B}$ is always perpendicular to the trajectory of the electron, therefore does not contribute to the change of the electron energy. Besides, the laser pulse with frequency ω_0 can propagate in the plasma provided the plasma density is less than the "critical density" n_c that is defined by

$$\omega_0^2 = \frac{e^2 n_c}{m_e \epsilon_0}, \tag{1.25}$$

which corresponds to a plasma density such that the nature oscillatory frequency of the

9

plasma is equal to the applied EM field frequency. As the nature frequency ω_p being higher than ω_0, the electrons can react to the external field and damp it away. This makes the EM wave can only propagate into the plasma with a skin depth $L_s = c/\omega_p$. On the other hand, if the plasma frequency is much smaller than the EM field frequency ($\omega_p \ll \omega_0$), referred to as "underdense plasma", the EM field can propagate inside the plasma.
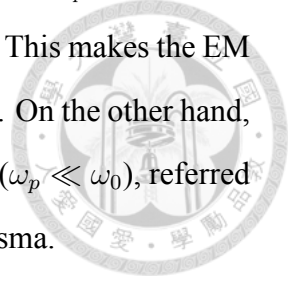
1.4 Particle In Cell Simulation

Traditionally, the investigations of phenomena in nature are carried out by experimental and theoretical techniques. Thanks to the rapid advance in computational power, computer simulation gradually becomes the third choice and benefits from the low cost compared to doing actual experiments and the ability to deal with complex physical systems. To numerically study the plasma behavior, there are two widely adopted methods. The first one is Magneto-hydrodynamics / Hydrodynamics (MHD/HD), in which the plasma is treated as fluid. The other one is particle-in-cell (PIC) simulation [30], where plasma is statistically sampled as macro-charged particles and the equation of motion is calculated kinetically. In general, MHD/HD methods are mostly used for investigating phenomenon of time scale larger than nanometer. On the other hand, PIC is for shorter time scale interaction, such as pico-second or femto-second , where the thermal equilibrium state is not arrived. In the scope of this thesis, the driver pulse is in fs scale and the interaction period is sub-ps. Therefore, we choose PIC as our numerical tool to study the laser plasma interaction.

PIC method combines the kinetic theory of plasma with Electromagnetic theory. Provided that the collision frequency between plasma is much smaller than the nature oscillation frequency of plasma, the system can be described by the collision-less Vlasov equation. In relativistic regime, the equation takes the form,

$$\left[\frac{\partial}{\partial t} + \frac{\mathbf{p}}{m_s \gamma} \cdot \frac{q_s(\mathbf{E} + \mathbf{v} \times \mathbf{B})}{m_s} \cdot \nabla_p\right] f_s(t, \mathbf{x}, \mathbf{p}) = 0, \tag{1.26}$$

where subscript s denotes species. In the implement of simulation code, the procedures

10

can be divided into two main parts: particle pusher and field solver. As the name suggests, particle pusher is responsible for moving particles with known electromagnetic force and field solver accounts for solving electromagnetic field from charge density and current. The routine of PIC simulation is summarized in Fig.(1.2).

In the following subsections, we briefly introduce the concept and algorithm used in PIC simulation.
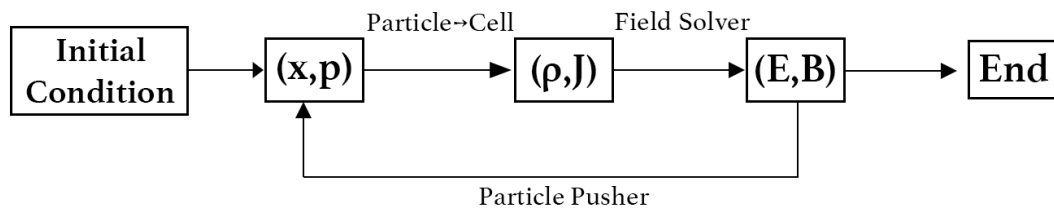
Figure 1.2: Schematic of PIC routine.

1.4.1 Finite Sized Particles

In principle, the particle simulation code should calculate the position and momentum of all particles in the system. However, even with the state-of-art supercomputer, it is impractical to consider interaction between 10^{20} particles, which is a typical number encountered in the plasma experiment. On the basis that the phenomena we usually concern about plasma are "collective" or "macroscopic" effect, huge amount of particles can be represented by a quasi-/pseudo-/macro- particle. This strategy drastically reduces the simulation particle numbers and makes computer simulation of plasma possible. Instead of treating the macro-particle as a point charge, finite sized particle is introduced. The reason comes from the fact that macro-particles overestimate Coulomb force, which is proportion to the multiplication of charge, among themselves and have divergent force in short range. Finite sized particles can eliminate the overestimation, more detail about this problem can be found in [30].

11

1.4.2   Field Solver

The electromagnetic fields $(\mathbf{E}, \mathbf{B})$ generated by charge density ρ and current $\mathbf{J}$ are described by Maxwell equations:

$$\nabla \cdot \mathbf{E} = \frac{\rho}{\epsilon_0} \tag{1.27}$$

$$\nabla \cdot \mathbf{B} = 0 \tag{1.28}$$

$$\nabla \times \mathbf{E} = \frac{\partial \mathbf{B}}{\partial t} \tag{1.29}$$

$$\nabla \times \mathbf{B} = \mu_0 \mathbf{J} + \frac{1}{c^2} \frac{\partial \mathbf{E}}{\partial t}. \tag{1.30}$$

To solve the field numerically, the problem domain is discretized into grids/cells. Several techniques for solving the electromagnetic field on the grids are available, e.g. finite-difference time-domain (FDTD), finite element method (FEM) and fast Fourier transform (FFT). The last two methods transform the partial differential equation problems into a global Eigen-value problem. Here, " global " means the solution of a specific point may depend on all the points in the problem domain. This property makes global field solver hard to be implemented efficiently in parallel computation. In modern PIC code, the widely used parallization technique, domain decomposition, demands the minimization of exchanging data between subdomains and implement of local equation solvers. Therefore, the FDTD method is in common use. The procedure begins with obtaining the density of plasma, which is extrapolated from the macro-particles onto the grid. After acquiring the density, the current can be evaluated with the help of continuity equation,

$$\nabla \cdot \mathbf{J} + \frac{\partial \rho}{\partial t} = 0. \tag{1.31}$$

Combining with Maxwell equations, electromagnetic field, which is discretized on the so-called Yee-grid [31], can be obtained. The detail of this algorithm can be found in the book [32].

12

1.4.3 Particle Pusher

The force experienced by a (relativistic) charged particle in electromagnetic field is described by the Lorentz force (cf. Eq.(1.23)). It should be noted that the fields are defined on the grid but particles are not. To calculate the field experienced by the macro-particles, the field should be interpolated to the position of particles first. After acquiring fields on each particle, the force can then be calculated. When updating the position of particles, the "leap-frog" scheme [33] is implemented :

$$\frac{x_{k+1} - x_k}{\Delta t} = v_{k+1/2} \tag{1.32}$$

$$\frac{v_{k+1/2} - v_{k-1/2}}{\Delta t} = \frac{q}{m}\left(\mathbf{E}_k + \frac{v_{k+1/2} + v_{k-1/2}}{2} \times \mathbf{B}_k\right) \tag{1.33}$$

The subscript k denotes the time steps. Velocity is defined at half-integer time steps, on the other hand, position and fields are defined at integer time steps. Therefore, the procedure of the scheme is: update half-step quantity (v) with full-step one (E, B), and then update full-step value (x) with half-step one (v). This method can prevent the numerical instability in the naive method, that is updating all quantities in integer time steps. The discussion about the stability with different updating strategy can be found in [34].

14

Chapter 2

Velocity of the Flying Mirror in Inhomogeneous Plasma

2.1 Introduction

The property of nonlinear plasma oscillation had been investigated in 1956 by Akhiezer and Polovin [35]. For the plasma wakefields (driven electron plasma waves) excited by an intense laser, a nonlinear one-dimensional theory was developed by Bulanov et al. [36]; Sprangle et al. [37, 38]; Berezhiani and Murusidze [39]. A set of coupled equations is derived to describe the vector potential of the laser field and the electrostatic potential of the plasma (wake potential). This model provides a self-consistent description of the interaction of intense laser with plasmas.

The wakefields can be a promising way to accelerate electrons due to its ability to sustain extremely large acceleration gradients. The scheme was first proposed by Tajima and Dawson [26], where the plasma wakefield is induced by the laser that traverses the plasma. Later, electron-bunch-driven accelerator was also proposed [40]. Among various laser plasma accelerator (LPA) configurations, the laser wake field accelerator (LWFA) is the most adopted scheme in modern LPA experiments. The phase velocity of the wake wave is a critical factor for determining the maximum energy gain, minimum injection energy, and the dephasing length of electrons. In an uniform plasma background, if the

15

evolution of driver is neglected as it propagates, the phase velocity of the plasma wave is equal to the group velocity of the driver, which is called the principle of wakefield. On the other hand, by introducing density gradient in the plasma background, the phase velocity is no longer equal to the group velocity and can be controlled artificially. This technique had been applied to fulfill the "self-injection" of electrons in LWFA [41, 42].

On the pure theoretical side, in 1993, Wilczek [13] suggested that a flying mirror can serve to investigate the information loss paradox [3] using suitable mirror trajectories. Based on this analogy, an experimental scheme was proposed by Chen and Mourou [20] with the intent to investigate the information loss paradox using a laser-induced plasma flying mirror in a tailored plasma target. By carefully designing the plasma density, different trajectories can be realized to mimic different candidate resolutions to the information loss paradox [19].

In this section, we start from reviewing the procedure to calculate the solution of wake potential induced by a nonlinear laser field. The solution exists when an optimal-length flat-top laser is considered. After that, the term "bubble width" is defined as the distance from the energy average position of driver and the first density cusp, that is the first flying mirror. This distance has been long considered as equal to the plasma wavelength. However, it is shown the ratio between bubble width and plasma wavelength is generally not equal to one. In the linear limit ($a_0 \to 0$), the ratio is found to be three quarters.

For an inhomogeneous plasma background, the optimal-length condition of the driver can not be maintained due to the change of local plasma density. We therefore extend previous studies on optimal-length to a driver with non-optimal length in Section 2.4. Unfortunately, a generally analytical solution can not be found in this case due to the inverse function appears in the solution is hard to be solved. However, as the driver is ultra-short, the approximated solution of wake potential can be found [37, 38]. Therefore, the ratio can be calculated and is found to be three quarters.

The bubble width ratio is important in calculation about the phase velocity of the flying mirror. In previous literature, based on the principle of wakefield, studies about the phase velocity of wake wave focuses on the nonlinear correction to the group velocity [43, 44,

45]. For an inhomogeneous plasma, the phase velocity of the wake wave was studied both analytically and numerically using the dispersion relation in [46]. This method focuses on the local phase velocity. On the other hand, another method which focuses on the velocity of the flying mirror is proposed in [21] recently. With the fact that the flying mirror is a bubble width behind the driver, if the rate of bubble size change can be known, the velocity of flying mirror can be obtained. Therefore, the bubble width should be carefully treated to acquire accurate result. In Section 2.5, we use this method and the derived formulae to calculate the velocity of flying mirror and compare with PIC data.

2.2 Wave Excitation by an Electromagnetic Pulse

To study the wakefield excited by an EM pulse, one can consider a 1D model based on cold relativistic hydrodynamics and Maxwell's equations. The plasma is assumed to be unmagnetised and ions are immobile. Consider the fluid is moving in z direction, the equation for electron momentum is

$$\frac{\partial \mathbf{p}}{\partial t} + v_z \frac{\partial \mathbf{p}}{\partial z} = -e(\mathbf{E} + \frac{1}{c}\mathbf{v} \times \mathbf{B}), \tag{2.1}$$

where $\mathbf{p} = m_0 \gamma \mathbf{v}$, $\gamma = \sqrt{1 + p^2/m_0^2 c^2}$, m_0 and $\mathbf{v}$ are the electron rest mass and velocity, respectively.

The electromagnetic field (from here referred as "driver") which propagates along z direction can be described by

$$\mathbf{E} = -\frac{1}{c}\frac{\partial \mathbf{A}_\perp}{\partial t} - \hat{z}\frac{\partial \phi}{\partial z}; \tag{2.2}$$

$$\mathbf{B} = \nabla \times \mathbf{A}_\perp, \tag{2.3}$$

where $\mathbf{A}_\perp = \hat{x}A_x + \hat{y}A_y$ is the vector potential and ϕ is the potential for charge separation in the plasma (also called wake potential). Note here that the Coulomb gauge is considered ($\nabla \cdot \mathbf{A} = 0$).

With Eq.(2.1)- (2.3), the perpendicular component of electron momentum can be found

17

to be

$$\frac{\mathbf{p}_\perp}{m_0 c} = \frac{e}{m_0 c^2} \mathbf{A}_\perp \equiv \mathbf{a}(z, t). \tag{2.4}$$

This shows the conservation of momentum in the transverse direction. The Lorentz factor can be separated into transverse and longitudinal direction:

$$\gamma = \left[1 + \left(\frac{p_\perp}{m_0 c} \right)^2 + \left(\frac{p_z}{m_0 c} \right)^2 \right]^{1/2} \equiv \gamma_a \gamma_\parallel, \tag{2.5}$$

where $\gamma_a = (1 + a^2)^{1/2}$ and $\gamma_\parallel = (1 - v_z^2/c^2)^{1/2}$ are the transverse and longitudinal gamma factor. To complete the description of the plasma fluid, we need the longitudinal component of Eq.(2.1), continuity equation, Poisson equation and the wave equation for the driver. The longitudinal component of Eq.(2.1) is,

$$\frac{1}{c} \frac{\partial}{\partial t} (\gamma_a \sqrt{\gamma_\parallel} - 1) + \frac{\partial}{\partial z} (\gamma_a \gamma_\parallel) = \frac{\partial \varphi}{\partial z}, \tag{2.6}$$

where $\varphi \equiv |e|\phi/m_0 c^2$ is the normalized scalar potential. The continuity equation is

$$\frac{1}{c} \frac{\partial n}{\partial t} + \frac{\partial}{\partial z} (n \beta_\parallel) = 0, \tag{2.7}$$

where $\beta_\parallel = v_z/c$. The Poisson's equation is,

$$\frac{\partial^2 \phi}{\partial z^2} = -4\pi\rho, \tag{2.8}$$

where ρ is the charge density. In the system, the ion is assumed to be immobile due to the large mass compared to electrons ($n_{ion} = n_0$ everywhere). Therefore, the charge density is $\rho = n_e - n_{ion} = n - n_0$. With the definition of ambient plasma wave number $k_p^2 \equiv 4\pi |e|^2 n_0 / m_0 c^2$, the Poisson equation can be written into

$$\frac{\partial^2 \varphi}{\partial z^2} = k_p^2 \left(\frac{n}{n_0} - 1 \right). \tag{2.9}$$

18

The wave equation is

$$\frac{\partial^2 \mathbf{A}}{\partial z^2} - \frac{1}{c^2}\frac{\partial^2 \mathbf{A}}{\partial t^2} = \frac{-4\pi}{c}\mathbf{J},\tag{2.10}$$

where the current $\mathbf{J} = n_0 e \mathbf{v}_\perp$. With the definition of normalized vector potential $\mathbf{a}$ and the conservation of transverse momentum (Eq.(2.4)), the equation can be reformed into,

$$c^2\frac{\partial^2 \mathbf{a}}{\partial z^2} - \frac{\partial^2 \mathbf{a}}{\partial t^2} = k_p^2\frac{n}{n_0}\beta_\perp = k_p^2\frac{n}{n_0}\frac{\mathbf{a}}{\gamma}.\tag{2.11}$$

It is convenient to transform from the lab frame coordinate (x,t) to a co-moving co-ordinate with the speed of the driver (ξ,τ), where $\xi = x - v_g t$ and $\tau = t$. The derivative in the co-moving coordinate is $\partial/\partial x = \partial/\partial \xi$ and $\partial/\partial t = \partial/\partial \tau - v_g \partial/\partial \xi$. With this transformation, Eq.(2.6),(2.7),(2.9) and (2.11) become

$$\frac{\partial}{\partial \xi}[\gamma(1 - \beta_g\beta_\parallel) - \varphi] = -\frac{1}{c}\frac{\partial}{\partial \tau}(\gamma_a\beta_\parallel),\tag{2.12}$$

$$\frac{\partial^2 \varphi}{\partial \xi^2} = k_p^2\left(\frac{n}{n_0} - 1\right),\tag{2.13}$$

$$\frac{\partial}{\partial \xi}[n(\beta_g - \beta_\parallel)] = \frac{1}{c}\frac{\partial n}{\partial \tau},\tag{2.14}$$

$$\left(\frac{1}{\gamma_g^2}\frac{\partial^2}{\partial \xi^2} + \frac{2\beta_g}{c}\frac{\partial}{\partial \xi \partial \tau} - \frac{1}{c^2}\frac{\partial}{\partial \tau^2}\right)\mathbf{a} = k_p^2\frac{n}{n_0}\frac{\mathbf{a}}{\gamma},\tag{2.15}$$

where $\beta_g = v_g/c$. Eq.(2.12)-(2.15) form a complete set of fully nonlinear, relativistic, cold fluid equations which describe the 1D laser-plasma interaction. The 1D model is valid provided that the spot size of driver is much larger than the plasma wavelength, i.e., $r_s \gg \lambda_p$. The set of equations can be further simplified with the so-called quasistatic approximation [37]. This approximation implies that if the laser pulse is sufficiently short, there exist a quasistatic state for the macroscopic quantities, n, $\beta_\parallel$ and γ. More explicitly, this approximation means that the right-hand side of Eq.(2.12) and (2.14) can be neglected, that is $\partial/\partial \tau \ll \partial/\partial \xi$ for the macroscopic quantities. In this case, the first integral of

19

Eq.(2.12) and (2.14) can be evaluated:

$$\gamma(1 - \beta_g \beta_\parallel) - \varphi = 1 \tag{2.16}$$

$$n(\beta_g - \beta_\parallel) = n_0 \beta_g, \tag{2.17}$$

with integration constant chosen such that for $\gamma_a = 1$, $n = n_0$, $\beta_\parallel = 0$, $\varphi = 0$. The initial condition means that when there is no driver field initially, no perturbation of density and wake potential exists. With Eq.(2.16) and (2.17), Eq.(2.12)-(2.15) can be reduced to,

$$\frac{d^2}{d\xi^2}\gamma(1 - \beta_g \beta_\parallel) = k_p^2 \frac{\beta_\parallel}{\beta_g - \beta_\parallel}, \tag{2.18}$$

$$2\frac{\partial}{\partial \tau}\left(i\omega_0 \mathbf{a}_0 + c\beta_0 \frac{\partial \mathbf{a}_0}{\partial \xi}\right) + c^2 \frac{\omega_{p0}^2}{\omega_0^2}\frac{\partial^2 \mathbf{a}_0}{\partial \xi^2} = -\omega_{p0}^2\left[1 - \frac{\beta_g}{\gamma(\beta_g - \beta_\parallel)}\right]\mathbf{a}_0. \tag{2.19}$$

In the ultra-relativistic limit ($\beta_g \approx 1$), the equations can be simplified (using the potential φ from Eq.(2.16)),

$$\frac{d^2\varphi}{d\xi^2} = \frac{k_{p0}^2}{2}\left[\frac{\gamma_a^2}{(1 + \varphi)^2} - 1\right] \tag{2.20}$$

$$2\frac{\partial}{\partial \tau}\left(i\omega_0 \mathbf{a}_0 + c\beta_0 \frac{\partial \mathbf{a}_0}{\partial \xi}\right) + c^2 \frac{\omega_{p0}^2}{\omega_0^2}\frac{\partial^2 \mathbf{a}_0}{\partial \xi^2} = -\omega_{p0}^2 \frac{\varphi}{1 + \varphi}\mathbf{a}_0. \tag{2.21}$$

These two equations together describe the evolution and coupling between the wake potential and the driving laser field.

2.3 Bubble Width with an Optimal-Length Pulse

The evolution of wake field which excited by a driver laser pulse can be described by the coupled equations discussed in previous subsection. Providing that the propagation distance is smaller than the depletion distance, the evolution of driver pulse can be neglected. Under this condition, the evolution of wake field can be simply described by Eq.(2.20). In the following derivation, we follow the notation and normalization using in [39]. The

20

equation for scalar potential (Eq.(2.20)) can be written in the form

$$\frac{\partial^2 y}{\partial x^2} = \frac{1}{2}\left(\frac{\gamma_{0\perp}^2}{y^2} - 1\right),$$

(2.22)

where $y \equiv 1 + \phi$, ϕ is the scalar potential, $\gamma_{0\perp}$ is the Lorentz factor of electron in perpendicular direction and $x = k_p \xi$ is the co-moving normalized spatial coordinate. For a linearly polarized driver pulse, $\gamma_{0\perp}^2 = 1 + a_0^2/2$ by conservation of transverse momentum. Here we consider a flat-top driver such that $\gamma_{0\perp} = \gamma_{0\perp}$ for $-L \leq x \leq 0$ and $\gamma_{0\perp} = 1$ elsewhere. The potential inside the driver ($-L \leq x \leq 0$) can be analytically solved as follows.

By multiplying $\frac{\partial y}{\partial x}$ on both sides of Eq.(2.22), we have

$$\frac{\partial y}{\partial x}\frac{\partial^2 y}{\partial x^2} = \frac{1}{2}\left(\frac{\gamma_{0\perp}^2}{y^2} - 1\right)\frac{\partial y}{\partial x},$$

(2.23)

which can be organized into

$$\frac{1}{2}[(y')^2]' = \frac{-1}{2}\left(\frac{\gamma_{0\perp}^2}{y} + y\right)'$$

(2.24)

Integrate both sides over x, we have:

$$(y')^2 = -\left(\frac{\gamma_{0\perp}^2}{y} + y\right) + C$$

(2.25)

where $C = 1 + \gamma_{0\perp}^2$ is the integration constant which can be determined by the boundary condition : $y(0) = 1, y'(0) = 0$. With the demand that real solution of y' exists $((y')^2 \geq 0)$, the value of y is bounded by

$$1 \leq y \leq \gamma_{0\perp}^2.$$

(2.26)

Eq.(2.25) can be written into

$$\frac{dy}{dx} = \pm\sqrt{\frac{(y-1)(\gamma_{0\perp}^2 - y)}{y}}$$

(2.27)

21

After integrating y from 1 to $\gamma_{0\perp}^2$ and x from 0 to x on both sides, we obtain the solution of y

$$x(y) = -2\gamma_{0\perp} E(\phi_i, \kappa_i) + 2\sqrt{\frac{(y-1)(\gamma_{0\perp}^2 - y)}{y}} \qquad (2.28)$$

where $E(\phi, \kappa)$ is elliptical integral of the second kind with argument $\phi_i \equiv \sin^{-1}\sqrt{\frac{\gamma_{0\perp}^2(y-1)}{(\gamma_{0\perp}^2-1)y}}$ and $\kappa_i \equiv \sqrt{\frac{\gamma_{0\perp}^2-1}{\gamma_{0\perp}^2}}$.

By substituting $y_{max} = \gamma_{0\perp}^2$ into Eq.(2.28), the maximum scalar potential is found at $x = -2\gamma_{0\perp} E(\kappa_i)$. Here $E(\kappa)$ is the complete elliptical integral of the second kind. This means the excited wake field becomes maximum when the flat-top pulse has an optimal length,

$$L = L_{opt} \equiv 2\gamma_{0\perp} E(\kappa_i). \qquad (2.29)$$

The scalar potential behind the pulse ($x \leq -L$) can be solved by noting that $\gamma_{0\perp} = 1$ due to the absence of driver pulse in this region. Therefore, Eq.(2.22) becomes

$$\frac{\partial^2 y}{\partial x^2} = \frac{1}{2}\left(\frac{1}{y^2} - 1\right) \qquad (2.30)$$

with boundary condition $y(x = -L_{opt}) = \gamma_{0\perp}^2$ and $y'(x = -L_{opt}) = 0$. With similar procedure above, the range and the solution of y in this region are

$$\frac{1}{\gamma_{0\perp}^2} \leq y \leq \gamma_{0\perp}^2 \qquad (2.31)$$

$$x(y) = -L_{opt} - 2\gamma_{0\perp} E(\phi_e, \kappa_e) \qquad (2.32)$$

where $\phi_e \equiv \sin^{-1}\sqrt{\frac{\gamma_{0\perp}^2(\gamma_{0\perp}^2 - y)}{\gamma_{0\perp}^4 - 1}}$ and $\kappa_e \equiv \sqrt{\frac{\gamma_{0\perp}^4-1}{\gamma_{0\perp}^4}}$. The longitudinal electric field is described by $E_\parallel = -dy/dx$ and has the form :

$$E_\parallel = \sqrt{\frac{\gamma_{0\perp}^4 + 1}{\gamma_{0\perp}^2} - \left(\frac{1}{y} + y\right)} \qquad (2.33)$$

22

The maximum $E_\parallel$ (sometimes referred to as the "wave-breaking" field) is given by minimizing $\frac{1}{y} + y$ in Eq.(2.33),

$$E_{\parallel,max} = \frac{\gamma_{0\perp}^2 - 1}{\gamma_{0\perp}} \tag{2.34}$$

The wavelength of plasma wave can be determined by the distance between adjacent maximum wake potential y in Eq.(2.32). Consider $y_{max} = \gamma_{0\perp}^2$, the argument of elliptic integral becomes $\phi_e(y_{max}) = \sin^{-1}(0) = n\pi$, where $n \in Z_0^+$. With the periodic property of elliptic integral of the second kind, $E(z + k\pi, m) = E(z, m) + 2\pi E(m)$, we have

$$E(0 + n\pi, \kappa_e) = E(0, \kappa_e) + 2nE(\kappa_e) = 2nE(\kappa_e). \tag{2.35}$$

Therefore, the position of first and second potential peak, which corresponds to $n = 0$ and $n = 1$ respectively, are

$$x_0 = -L_{opt} \tag{2.36}$$

$$x_1 = -L_{opt} - 4\gamma_{0\perp}E(\kappa_e) \tag{2.37}$$

After recovering the normalization constant, the non-linear wavelength of the wake wave is [39]

$$\lambda_{NP} = \left| \frac{x_1 - x_0}{k_p} \right| = \frac{4\gamma_{0\perp}c}{\omega_p}E(\kappa_e) = \frac{2\gamma_{0\perp}E(\kappa_e)}{\pi}\lambda_p \tag{2.38}$$

In non-relativistic limit ($\gamma_{0\perp} \to 1$), $E(\kappa_e) \to \pi/2$, the definition of linear plasma wavelength is recovered ($\lambda_{NP} \to \lambda_p$).

With the definition of the plasma wavelength, we can discuss the problem of "Bubble width". In our context, "Bubble width" is defined as the distance between driving laser pulse and the position of first maximum density perturbation. Usually, this distance is treated as the plasma wavelength (Eq.2.38). However, in the following, we demonstrate that there is a factor between plasma wavelength and bubble width. This factor plays an important role when calculating the phase velocity of the flying mirror.

Position of driver can be defined as the energy average position,

$$x_L \equiv \frac{\int x E_\perp^2 dx}{\int E_\perp^2 dx} \tag{2.39}$$

where $E_\perp$ is the amplitude of electric field of driver. Position of mirror is at where $E_\parallel = 0$ with $\partial E_\parallel / \partial x < 0$.

For a flat-top driver with optimal length, the energy average position is,

$$x_L = \frac{\int_0^{-L_{opt}} x \cdot a_0^2 dx}{\int_0^{-L_{opt}} a_0^2 dx} = -\frac{L_{opt}}{2}. \tag{2.40}$$

The position of mirror is at where $y = \frac{1}{\gamma_{0\perp}^2}$, $\phi_e = \sin^{-1}(\pm 1) = \pi/2 + n\pi$. $n = 0, 1, 2...$ corresponds to the first, second ... peak density. Therefore, the position of first density peak is at

$$x_{p1} = -L_{opt} - 2\gamma_{0\perp}E(\kappa_e) \tag{2.41}$$

The distance between driver and first density is

$$x_L - x_{p1} = \frac{L_{opt}}{2} + 2\gamma_{0\perp}E(\kappa_e). \tag{2.42}$$

After putting normalization factors back and using the definition of L_{opt}, we have the definition of bubble width,

$$\lambda_B = \frac{c}{\omega_p}[\gamma_{0\perp}E(\kappa_i) + 2\gamma_{0\perp}E(\kappa_e)]. \tag{2.43}$$

Compare with plasma wavelength,

$$\lambda_B = \frac{\gamma_{0\perp}E(\kappa_i) + 2\gamma_{0\perp}E(\kappa_e)}{2\pi} * \lambda_p \equiv \alpha\lambda_p. \tag{2.44}$$

Note that the definition of bubble width differs from the non-linear plasma wavelength (cf. Eq.(2.38)). Generally speaking, the ratio α between λ_p and λ_B doesn't equal to one.

24

Consider the linear limit ($\gamma_{0\perp} \approx 1$, $E(\kappa_i) \approx E(\kappa_e) \approx \pi/2$), we have :

$$\lambda_B \approx \frac{3}{4}\lambda_p \text{ as } \gamma_{0\perp} \to 1. \tag{2.45}$$

This implies that in the linear limit, the bubble width is only three quarters of the plasma wavelength. The factor $3/4$ can be understood as follows. In Fig.(2.3), the solution of the wake potential and density perturbation are numerically obtained with a linear optimal-length flat-top driver. The auxiliary vertical grey dash lines are separated equally by $\lambda_p/2$. In the linear limit, the optimal-length $L_{opt} = 2\gamma_{0\perp}E(\kappa_e)/k_p \approx \lambda_p/2$. Accordingly, the energy average position of driver is at $x_L = -L_{opt}/2 = -\lambda_p/4$. The end point of the driver is the first peak of the wake potential. Besides, the first peak of density perturbation, or the first mirror, is at where wake potential is minimum. This implies the distance from the end point of driver to the first mirror is half the wavelength of wake wave. Therefore, the distance between the driver and the first mirror is $\lambda_p/4 + \lambda_p/2 = 3/4\lambda_p$.
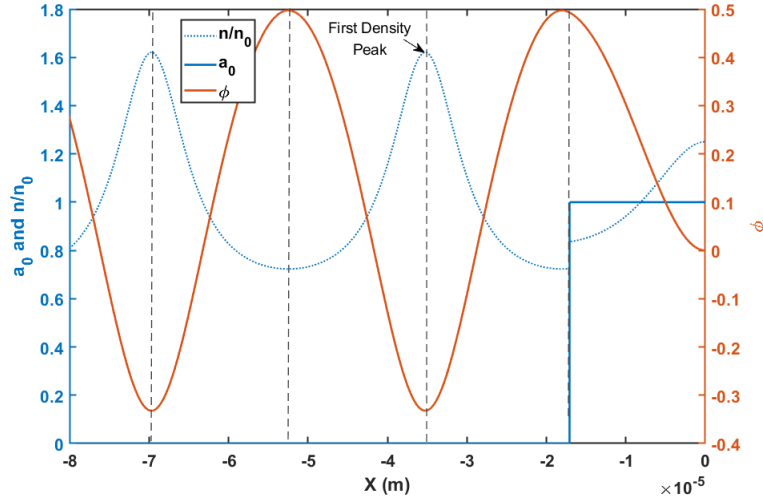

Figure 2.1: Wake wave potential with an optimal-length driver in linear limit. The bubble width is three quarters of linear plasma wavelength.

2.4 Bubble Width with a Non-Optimal-Length Pulse

In the previous section, we discuss the analytical solution of wake wave equation with an optimal-length flat-top driver. However, the optimal-length condition is hard to maintain

25

in the scheme that controls phase velocity through graded background plasma density [46, 21]. The optimal-length, Eq.(2.29), depends on k_p, or on the background plasma density. Therefore, a fixed pulse length driver, which is an usual case in experiment, can not maintain optimal as graded density presented.

Here, we extend previous studies on an optimal-length flat-top laser to a non-optimal one. The coupled wave equation with non-optimal-length pulse can be solved by separating the solution domain into three regions as Fig.(2.4) shows. Consider a flat-top laser with arbitrary pulse length L.

$$
a = \begin{cases} a_0 & \text{for } -L \leq x \leq 0 \\ 0 & \text{x elsewhere.} \end{cases} \tag{2.46}
$$

Region I corresponds to where driver pulse exists and the end point is denoted as B. Region III starts at point A where the spatial derivative of potential equals to 0, that is $y' = (1 + \phi)' = 0$. For an optimal-length pulse, the pulse length L is chosen such that the potential at the end of driver is maximum, which means point B is same as A. On the other hand, for a non-optimal-length driver, there exists a region between A and B. We denote this zone as region II.
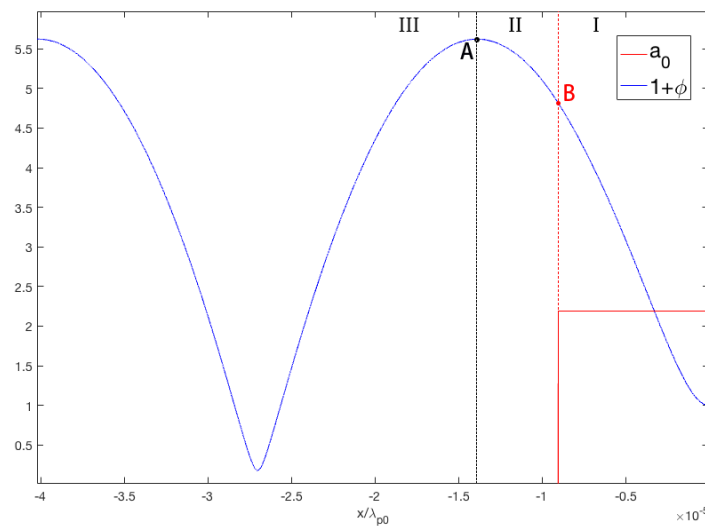

Figure 2.2: Solution domain of the wakefield with a non-optima-length driver pulse. The domain is separated into three regions.

Analytical solutions of y in region I and III exist. In region I, by considering the initial

26

condition : $y_{x=0} = 1, y'_{x=0} = 0$, the solution is the same as Eq.(2.28). The potential in both region II and III satisfy Eq.(2.30) due to the absence of laser field. With initial condition $y_{x=x_A} = y_A$, $y'_{x=x_A} = 0$, the solution in region III is,

$$x = -x_A - 2\sqrt{y_A}E(\phi_e, \kappa_e), \tag{2.47}$$

where $\phi_e \equiv \sin^{-1}[\sqrt{\frac{y_A(y_A-y)}{y_A^2-1}}]$, $\kappa_e \equiv \sqrt{\frac{y_A^2-1}{y_A^2}}$ and y_A is a constant that is determined by solutions in region I and II.

In region II, after integrating both sides of Eq.(2.30), we have

$$y'^2 = C - (\frac{1}{y} + y), \tag{2.48}$$

where C is the constant of integration. With the initial condition at point B : $y_{x=x_B} = y_B$ and $y'_{x=x_B} = y'_B$, the constant C is :

$$C = y'^2_B + \frac{1}{y_B} + y_B. \tag{2.49}$$

With Eq.(2.48).(2.49), the value of y is bounded by

$$\frac{C - \sqrt{C^2 - 4}}{2} \leq y \leq \frac{C + \sqrt{C^2 - 4}}{2}. \tag{2.50}$$

The upper (lower) bound corresponds to the maximum (minimum) value of y in the case $L < L_{opt}$ ($L > L_{opt}$). According to the definition that y_A is the extreme value ($\because y'_A = 0$), we know,

$$y_A = \begin{cases} \dfrac{C + \sqrt{C^2 - 4}}{2}, L < L_{opt} \\ \dfrac{C - \sqrt{C^2 - 4}}{2}, L > L_{opt}. \end{cases} \tag{2.51}$$

The solution of y is symmetric about point A in region II and III. Therefore, y_B also satisfies Eq.(2.47)

$$x_B = -x_A - 2\sqrt{y_A}E(\phi_f, \kappa_f), \tag{2.52}$$

27

where $\phi_f \equiv \sin^{-1}[\sqrt{\frac{y_A(y_A - y_B)}{y_A^2 - 1}}]$ and $\kappa_f \equiv \sqrt{\frac{y_A^2 - 1}{y_A^2}}$. By defining the length of region II as $L_{II} \equiv |x_B - (-x_A)|$ and put the normalization factor back, we have

$$L_{II} = \frac{2\sqrt{y_A} E(\phi_f, \kappa_f)}{k_p}. \tag{2.53}$$

As discussed in the optimal-length driver case, the energy average position of a flat-top laser is at $L/2$ and the distance between x_A and first density peak is $2\sqrt{y_A}E(\kappa_e)/k_p$. Therefore, the bubble width with non-optimal-length pulse is the sum of above two distance and the length of region II,

$$\lambda_B = \frac{L}{2} + \frac{2\sqrt{y_A}[E(\kappa_e)]}{k_p} + \frac{2\sqrt{y_A}E(\phi_f, \kappa_f)}{k_p} \tag{2.54}$$

$$= \left(\frac{L}{2\lambda_p} + \frac{\sqrt{y_A}[E(\kappa_e) + E(\phi_f, \kappa_f)]}{\pi} \right) \lambda_p \equiv \alpha \lambda_p \tag{2.55}$$

In above equations, λ_B depends implicitly on y_B through Eq.(2.49), (2.51). Generally speaking, y_B is hard to be solved analytically from Eq.(2.28), therefore λ_B need to be determined by numerical method. However, in the ultra-short pulse limit ($L \ll \lambda_p$), analytical form of λ_B can be found.

2.4.1 Ultra-Short Pulse Limit

Each term in the right hand side of Eq.(2.55) are treated respectively. The first term $L/2\lambda_p$ can be safely drop under the ultra-short limit ($L/\lambda_p \ll 1$). The second term depends on the constant C, y_B and y_B' through the argument κ_e. It is shown in [37, 38] that as long as $L \ll \lambda_p$, the wake potential $y = 1 + \phi \approx 1$ in region $-L \leq x \leq 0$. This implies $y_B \approx 1$ and $y_B' \approx 0$. Besides, this result can be extended to driver pulse with shape other than flat-top. For a pulse with envelope given by $a = a_0 \sin(\pi x/L)$ for $-L \leq x \leq 0$ and $a = 0$ otherwise, the wake potential is $y|_{x=-L} = (a_0 k_p L/4)^2$. It should be noted here that a driver with delta function shape $a = \delta(x)$ apparently satisfies $L \ll \lambda_p$ but may break the conclusion, $y_B \approx 1$, due to the infinity electric field in the origin. Therefore, we may generalize the ultra-short pulse constraint to $(a_0 k_p L/4)^2 \ll 1$ to include the effect of a_0.

28

With the approximation ($y_B \approx 1$ and $y_B' \approx 0$), Eq.(2.49) and (2.51) give $C = y_B'^2 + \frac{1}{y_B} + y_B \approx 2$ and

$$y_A = \frac{C + \sqrt{C^2 - 4}}{2} \approx 1. \tag{2.56}$$

With $\kappa_e \approx 0$ in this limit, the second term becomes

$$\frac{\sqrt{y_A} E(0)}{\pi} \approx \frac{1}{2}. \tag{2.57}$$

Furthermore, $\kappa_f \approx \sin^{-1}(0) = 0$, $\phi_f \approx \pi/4$. The third term is therefore,

$$\frac{\sqrt{y_A} E(0, \pi/4)}{\pi} \approx \frac{1}{4}. \tag{2.58}$$

To sum up, under the ultra-short pulse limit the analytical form of λ_B is,

$$
\begin{aligned}
\lambda_B &= \left(\frac{L}{2\lambda_p} + \frac{\sqrt{y_A}[E(\phi_f, \kappa_f) + E(\kappa_e)]}{\pi} \right) \lambda_p \\
&\approx \frac{3}{4} \lambda_p.
\end{aligned}
\tag{2.59}
$$

In Fig.(2.4.1), ϕ and n/n_0 are solved with an ultra-short sin driver with $L/\lambda_p = 0.05$. Under the ultra-short pulse condition, the driver hardly excite the wake wave. It is clear that the distance from the driver, at the origin, to first density peak is three-quarters of the wake wave. Let us refer the region where ϕ goes from 0 to the first maximum as region A. In the optimal-length case, region A is prolonged to be $\lambda_p/2$ with driver at $\lambda_p/4$. On the other hand, the region A remains the same length $\lambda_p/4$ here with driver at the origin. Therefore, the factor "three quarters" appears in both case but are from different reasons. It should be noted that the wake is not excited efficiently under ultra-short-pulse condition, actually this is the physical meaning of $y_B \approx 1$. This is more clear when we consider the equation of scalar potential. As $\phi \to 0$, Eq.(2.22) becomes

$$\frac{\partial^2 y}{\partial x^2} = \frac{1}{2}(\gamma_{0\perp}^2 - 1). \tag{2.60}$$

29

The solution of y will be just a sinusoidal function, no nonlinear effect exists. Therefore, the ultra-short pulse limit makes analytical calculation simple but may need to be avoided when an intense electron flying mirror is needed.
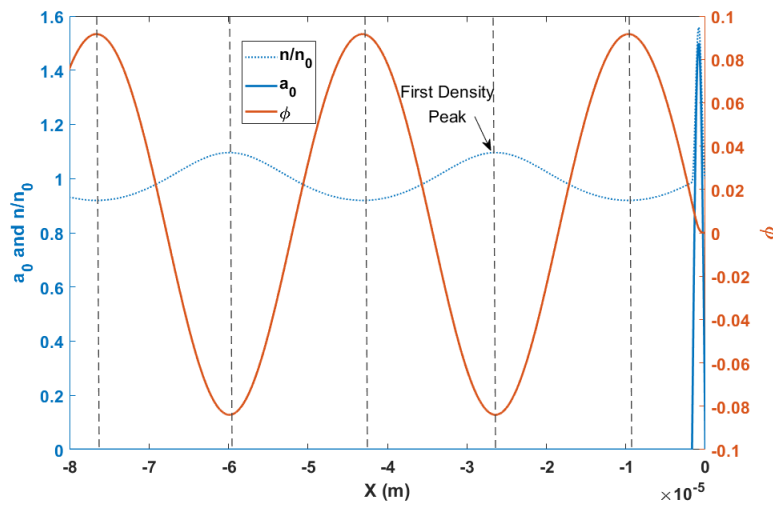
Figure 2.3: Wake wave potential with an ultra-short driver. The bubble width is shown to be three quarters of the plasma wavelength.

2.5 Phase Velocity of the Flying Mirror

The phase velocity of the wake field plays an important role in wakefield accelerators. The roles include the accelerated length and the injection mechanism of electrons. Bulanov et al. proposed an self-injection mechanism [41] based on the fact that down-ramp plasma background can reduce the phase velocity of wake field. As Wave breaking happened, that is when the phase velocity equals to the quiver velocity of electrons, electrons will be trapped into the wakefield. The trapped electrons are from the background plasma rather than an external source in this scheme, therefore is termed as "self-injection". In this scheme, to determine whether or when the wave breaking happened, a robust relation between background plasma density and the phase velocity is needed. In the following text, we briefly introduce two different ways to calculate the phase velocity and how the factor α between plasma wavelength and bubble width corrects the result.

The first method is using the dispersion relation of the plasma wave. In [46], the phase velocity under an inhomogeneous plasma is discussed. Consider the eikonal of the plasma

30

wave $\theta(x,t)$, the angular frequency ω_p and wave number k_p are, $\omega_p = -\partial_t\theta$, $k_p = \partial_x\theta$ respectively. With the cross differentiation property, frequency and wave number have such relation,

$$\partial_t k_p = -\partial_x \omega_p. \tag{2.61}$$

After integrating over t, this gives $k_p = k_{p,0} - \partial_x\omega_p$, where $k_{p,0}$ is the initial wave number. Phase velocity, defined as $v_{ph} = \omega_p/k_p$, is therefore

$$v_{ph} = \frac{\omega_p}{k_{p,0} - \partial_x\omega_p}. \tag{2.62}$$

The plasma frequency ω_p depends on the local electron density, $\omega_p(x) = \sqrt{\frac{n_e(x)e^2}{m_e\epsilon_0}}$. In a mildly graded plasma, that is $|\partial_x\omega_p|$ is small,

$$v_{ph} \approx v_{ph,0}\left(1 + \sqrt{\frac{e^2}{m_e\epsilon_0}}\frac{t}{k_{p,0}}\partial_x\sqrt{n_e}\right). \tag{2.63}$$

For a down ramp density profile, $\partial_x\sqrt{n_e} < 0$, the phase velocity decrease with time.

The other method to calculate phase velocity is proposed in [21]. As we discussed in previous subsection, the flying mirror is a bubble width behind the driver. Therefore, the position of flying mirror can be described by

$$x_M = x_L - \lambda_B, \tag{2.64}$$

where x_M and x_L are the position of flying mirror and the driver respectively. Let $\dot{x} \equiv dx/dt$, the velocity of mirror is then

$$\dot{x_M} = \dot{x_L} - \dot{\lambda_B}. \tag{2.65}$$

This shows that the velocity of the flying mirror depends on the velocity of driver and the variation of the bubble width. In a homogeneous plasma, the bubble width can be treated as a constant provided that the depletion of driver can be neglected. This leads to the

31

velocity of flying mirror equals to the group velocity, which is the *principle of wakefield*. However, in an inhomogeneous plasma, with $d/dt = \partial/\partial t + \dot{x_M}\partial/\partial x$, we can write the velocity of mirror as

$$\dot{x}_M = \frac{\dot{x}_L}{1 + \lambda'_B}.$$ (2.66)

Recall that the bubble width can be described by $\lambda_B = \alpha\lambda_p$ (cf. Eq.(2.44)), the velocity can be written as

$$\dot{x}_M = \frac{\dot{x}_L}{1 + \alpha\lambda'_p + \alpha'\lambda_p}.$$ (2.67)

In general, α is a function of the position of flying mirror when graded background density is presented. In Fig.(2.4), we show the numerical result about the relation between α and the ratio between driver pulse length and the ambient plasma wavelength L/λ_p. As mentioned in the non-optimal-length case, the ratio L/λ_p varies for a fixed length driver in an inhomogeneous plasma background. This makes α not a constant.
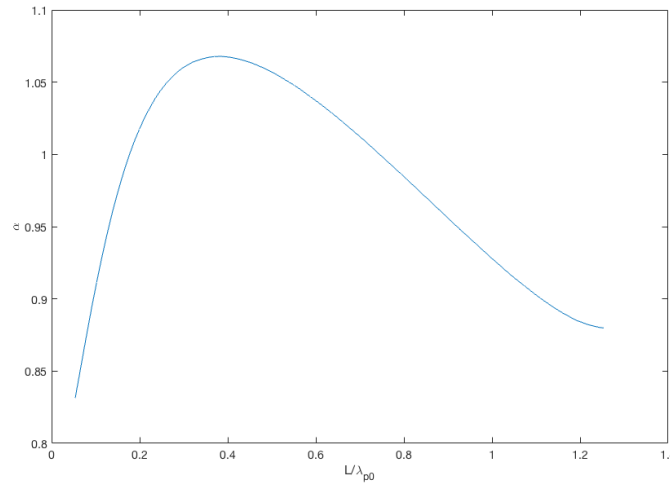

Figure 2.4: Dependence of α on the normalized pulse length.

Therefore, for an arbitrary density profile and pulse length, numerically solving Eq.(2.55) and Eq.(2.66) is needed. In Fig.(2.5), a flat-top driver with fixed pulse duration $L/c =$

32

$47.5 fs$ is used. The background density profile is

$$n(x) = n_0 \left(1 + e^{-x^2/2D^2} \right)^2, \tag{2.68}$$

with $n_0 = 10^{24} m^{-3}$ and the characteristic length $D = 100 \mu m$. The numerical result agrees well with 1D PIC simulation data.
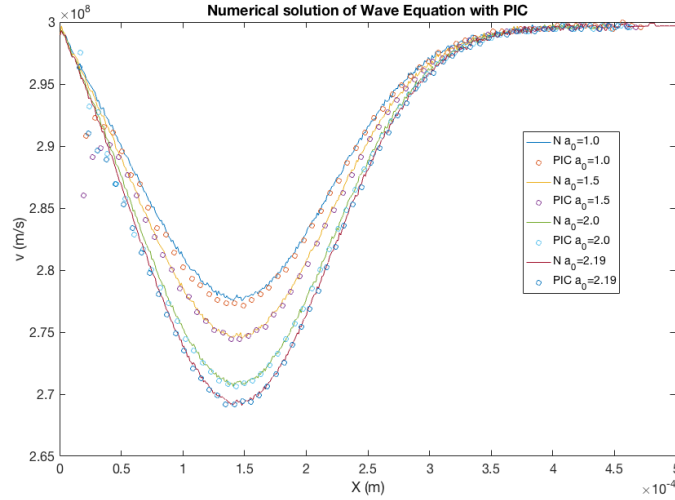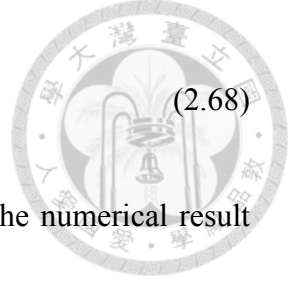
Figure 2.5: Comparison between PIC data and theoretical results of velocity of the flying mirror. Curves are calculated numerically from Eq.(2.55), (2.66). Circles are PIC simulation data. Driver with different a_0 are considered.

As we find previously, α equals to a constant $3/4$ in two limits. The first one is a non-relativistic optimal-length driver. However, this approximation is not valid in a graded plasma background because the optimal condition can not be maintained. The other one is the ultra-short pulse limit. Even for a graded plasma, the condition can be satisfied provided that $L \ll \lambda_p$.

Consider the Gaussian-like down-ramp density profile (Eq.(2.68)). To satisfy the ultra-short approximation, the FWHM pulse length L of the gaussian driver is chosen such that $L \ll \lambda_p$. The condition guarantees $\alpha = 3/4$. With Eq.(2.67), Eq.(2.68) and applying the underdense approximation ($\omega_p^2/\omega_0^2 \ll 1$), the velocity of mirror can be described by [21]

$$\frac{\dot{x_M}}{c} = \frac{1}{1 + (3b/2)(\lambda_{p0}\, x/D^2)e^{-x^2/2D^2}}. \tag{2.69}$$

1D PIC simulations are performed to verify the predictive ability of Eq.(2.69) with pa-

33

rameters: $n(0) = 4n_0 = 1.0 \times 10^{23} m^{-3}$, $D = 100\mu m$. The simulations are separated into two groups. The first one is fixing $L = 2.4\mu m$ but varying the intensity of driver with $a_0 = 1.5, 2.1, 2.19, 2.5$. The second group is fixing the intensity of driver to $a_0 = 2.0$ but varying the pulse duration $L/c = 4, 6, 10, 14, 20, 25, 30 fs$. The comparison between analytical results (Eq.(2.69)) and 1D PIC simulation is shown in Fig.(2.6). The subplot (a) demonstrates the comparison among analytical prediction with $\alpha = 1$ and $\alpha = 0.75$ and 1D PIC data with driver pulse of different a_0. The curve with $\alpha = 0.75$ agrees well with PIC data for cases of different a_0. The subplot (b) shows the agreement between analytical curve and PIC data with different length driver. This verifies the argument that as long as ultra-short pulse limit holds, $\lambda_B = 0.75\lambda_p$ is a good approximation.

In the end of this section, we hope to discuss about the two different methods when applied to compute the velocity of the flying mirror. They are

$$\dot{x_M} = \frac{\dot{x_L}}{1 + \lambda'_B}, \tag{2.70}$$

$$v_{ph} = \frac{v_{ph,0}}{1 - \frac{\partial \omega_p}{\partial x} \frac{t}{k_{p,0}}}. \tag{2.71}$$

As we demonstrated earlier, Eq.(2.70) can provide well prediction about the velocity of flying mirror. Here, we wonder whether Eq.(2.71) gives the same result. The $v_{ph,0}$ in the numerator is the phase velocity in the homogeneous region. Based on the wake field principle, we know the velocity of the mirror can be approximated with the velocity of driver pulse, that is $\dot{x_L}$. For the denominator, first we need to clarify the meaning of t. The $time$ here means the time after the wake wave formed. In the scheme of laser-driven wakefield, the wake wave is induced by the driver pulse. Therefore, the time t corresponds to how long after the driver pulse passed. Here, we are discussing about the first flying mirror. According to the result in previous sections, the first mirror always trails behind the laser by a distance $3/4\lambda_p$ under ultra-short pulse condition. This implies $t = (3/4)(\lambda_p/c)$. Other terms in the denominator can be rewritten as $\partial \omega_p / \partial x = -2\pi c / \lambda_p^2 \lambda'_p$ and $1/k_{p,0} =$

34
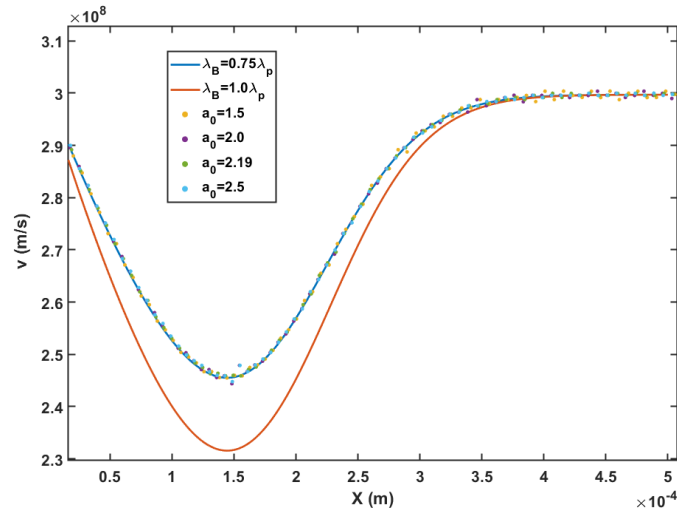
(a) Driver with different a_0
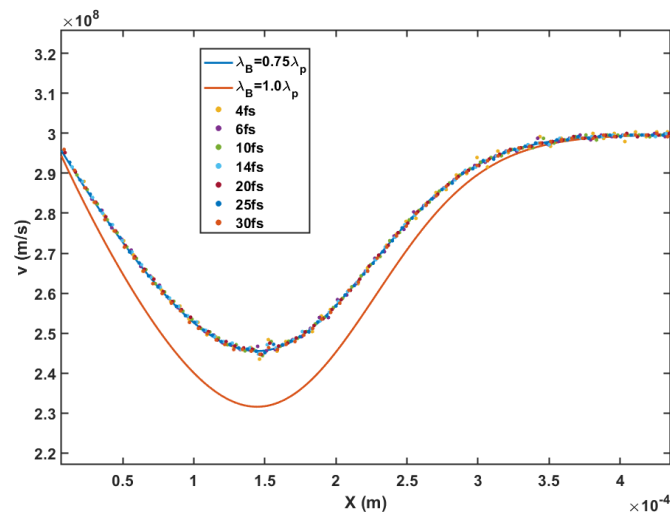
(b) Driver with different L

Figure 2.6: Phase velocity of the flying mirror in a gaussian down-ramp plasma background. Solid lines are analytical predictions. Dots are 1D PIC data. It can be seen that $\alpha = 3/4$ is a good approximation as long as the ultra-short pulse condition holds.

35

$\lambda_p / 2\pi$. After putting these terms back into Eq.(2.71), we get

$$v_{ph,M} = \frac{\dot{x_L}}{1 + 3/4\lambda_p'} \qquad (2.72)$$

which recovers Eq.(2.70) in the ultra-short pulse limit. A short conclusion is that these two methods are consistent with each other but focus on different face. Eq.(2.70) cares mainly about the flying mirror, it is more straightforward and easily-implemented if the problem is about the flying mirror like the study of trajectory of the mirror [21]. On the other hand, Eq.(2.71) can describe the phase velocity of all parts in the wake wave. This is useful in the discussion of electron self-injection scheme because we are only curious about "whether" but not "where" the electrons are injected [46].

2.6 Conclusion

In this section, we investigate the bubble width which is defined as the distance between the driver and the flying mirror based on the coupled equations of laser-driven wakefield. We showed that the bubble width differs from the plasma wavelength. In certain limit, the ratio between bubble width and plasma wavelength can be found analytically. Such as the wakefield excited by a linear optimal-length driver or an ultra-short-pulse driver, the ratio is found to be three quarters. Furthermore, we examine two different methods to calculate the velocity of the flying mirror and show the equivalence between these two procedures. These studies can help to calculate the velocity of flying mirror in an inhomogeneous plasma background. This may benefit the design of plasma density profile to realize different trajectories which can mimic different evolution of black holes.

36
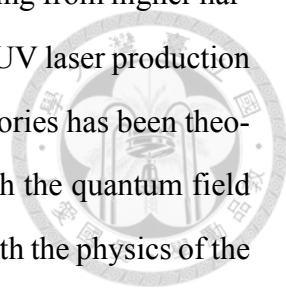
Chapter 3

Reflectivity and Reflected Spectrum of a Relativistic Flying Mirror

3.1 Introduction

In 1905, Einstein first studied [47] the interaction between light and a reflecting mirror moving with arbitrary velocity in vacuum. Since then, the concept of flying mirrors has attracted wide attention for theoretical and experimental applications. An optical laser pulse reflected from such a relativistic flying plasma mirror would not only upshift its frequency by a factor $4\gamma^2$, where γ is the Lorentz factor of the mirror but also reduce its diffraction-limited volume due to the much shorter reflected wavelength.

Relativistic flying mirror can be generated from irradiating an intense laser pulse on a plasma target. Such a plasma mirror is composed of a dense electron thin shell that moves with relativistic velocity. There are different mechanisms proposed to generate relativistic flying mirrors. Among them the idea of using the plasma wakefield [26, 40] in the nonlinear perturbation regime as a relativistic flying plasma mirror [48] is particularly attractive. This scheme had been experimentally proven to be feasible by Kando et al. [49, 50, 51]. Other ideas include, e.g. double-sided mirror [52], oscillating mirror [53], sliding mirror [54], nonlinear Langmuir waves [55, 56], and electron density singularities [57]).

The relativistic flying mirror has wide practical applications, ranging from higher harmonic generation (HHG) [55], attosecond pulse generation [56], to XUV laser production [49, 50]. On the pure physics side, flying mirror with different trajectories has been theoretically investigated as a model to mimic phenomena associated with the quantum field theory in curved spacetime [11, 58, 12], which is closely associated with the physics of the black hole Hawking radiation [2]. On the basis of this theoretical analogy, an experimental scheme was recently proposed by Chen and Mourou [14] with the intent to investigate Hawking evaporation through laser-driven relativistic flying plasma mirrors. In the proposal, an underdense plasma target with a tailored density gradient is invoked to realize a desired trajectory of the flying plasma mirror [59]. Currently, there is an on-going project, AnaBHEL (Analog Black Hole Evaporation via Lasers) that attempts to carry out such an experiment. If realized, it may help to shed more lights on the solution to the long-standing information loss paradox [3].

Considering the reality that flying plasma mirrors tend to have a low reflectivity [60] and with a finite size, which deviate from the highly idealized theoretical studies in the literature, the analog Hawking radiation spectrum from flying plasma mirrors with a partial reflectivity and finite dimensions have been calculated recently [61, 62], which should help to guide the design of the AnaBHEL experiment. To measure the trajectory of a flying mirror, which is closely related to the characteristic temperature of the Hawking radiation, the velocity of the plasma mirror at different instants (therefore different locations) should be measured so as to cross compared with the detected analog Hawking radiation spectrum.

To reconstruct the flying mirror trajectory and its relation to the reflected Hawking spectrum, the reflectivity and the Lorentz factor of the plasma mirror should be carefully studied. Bulanov et al. have analytically investigated the reflectivity of a near-wave-breaking flying plasma mirror using the collisionless cold plasma theory [60]. From our one-dimensional particle-in-cell (1D PIC) simulations, we found that the formula of Bulanov et al. tends to overestimate the reflectivity. We therefore propose a fitting model based on the PIC data. This model can provide better prediction about the reflectivity of

38

the flying plasma mirror. Furthermore, we extend the previous study on the interaction between a flying mirror and a plane wave to an incident wave with a finite bandwidth, which is closer to a realistic experimental setup. The peak frequency of the reflected spectrum from an incident wave with a Gaussian temporal profile is found to be deviated from the standard value of $[(1+\beta)/(1-\beta)]\omega_s$ due to the dependence of the reflectivity on the incident wave (source) frequency ω_s. We suggest that the deviation can be treated as a correction term, which may serve to improve the precision of the Lorentz factor derived from the reflection spectrum.

This section is organized as follows: in Section 3.2 we review previous studies on the reflectivity and propose a new model based on the numerical fitting of our PIC simulation data, which is different from that based on the near-wave-breaking condition. The validity of different density models are examined by analyzing the reflectivity of the flying mirror through 1D PIC simulations. Furthermore, we briefly describe the feasibility of generating water window X-ray from a relativistic flying mirror in underdense plasma. In Section 3.3 we discuss the reflected spectrum of the incident wave with Gaussian temporal profile and compare theoretical calculations with 1D PIC simulation results.

3.2 Reflectivity of a Flying Mirror

The reflectivity of a relativistic flying plasma mirror has been studied by Bulanov [60] and H.-C Wu [63]. Their procedures are different but construct the same relation between density profile of electrons and the reflectivity. Here, we first introduce Bulanov's method and then the one proposed by H.-C Wu.

Consider the electromagnetic wave polarized in z direction and propagates along x axis. The vector potential $A_z(x,t)$ satisfies the wave equation

$$\frac{\partial^2 A_z}{\partial t^2} - c^2 \frac{\partial^2 A_z}{\partial x^2} + \omega_p^2 A_z = 0, \tag{3.1}$$

39

where ω_p is the plasma frequency. Consider A_z is in the form

$$A_z = A_z(x)e^{-i\omega_0 t},$$

(3.2)

Eq.(3.1) becomes

$$\frac{\partial^2 A_z}{\partial x^2} + \frac{\omega_0^2 - \omega_p^2}{c^2} A_z = 0.$$

(3.3)

After normalizing by defining $a(x) = eA_z(x)/m_e c^2$ and performing the Lorentz transformation to a frame moving with phase velocity of the plasma wave, which is defined by $\zeta = \gamma_{ph}(x - v_{ph}t)$. Eq.(3.3) then becomes

$$\left[\frac{d^2}{d\zeta^2} + \frac{(\omega_0')^2 - \omega_p'^2(\zeta)}{c^2}\right] a(\zeta) = 0,$$

(3.4)

where " $'$ " denotes quantities in mirror's proper frame. We can represent the solution to Eq.(3.4) as

$$a(\zeta) = b_+ \exp(is\zeta) + b_- \exp(-is\zeta),$$

(3.5)

where $s \equiv \omega_0'/c$ and $b_+(\zeta)$ and $b_-(\zeta)$ are the amplitudes of reflected and transmitted waves. In the limit $\zeta \to -\infty$, $b_+(\zeta)$ is the amplitude of the incident wave and $b_-(-\infty) = \rho$ is the amplitude of the reflected wave. For $\zeta \to +\infty$, $b_+(\infty)$ is equal to the amplitude of transmitted wave and $b_-(\infty) = 0$. Therefore, with definition of the reflective and transmit coefficient **R** and **T**, we have $|b_+(-\infty)|^2 = 1$, $|b_-(-\infty)|^2 = \mathbf{R}$, $|b_+(\infty)|^2 = T$ and $b_-(\infty) = 0$.

Because two unknown functions $b_+(\zeta)$ and $b_-(\zeta)$ are introduced, instead of one $a(\zeta)$, we need to impose extra conditions on the solution. The derivative of vector potential is required to satisfy
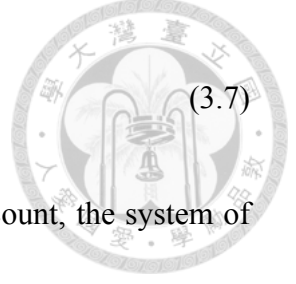
$$\frac{da}{d\zeta} = is[b_+(\zeta)\exp(is\zeta) - b_-(\zeta)\exp(-is\zeta)],$$

(3.6)

40

that is

$$\frac{db_+}{d\zeta}\exp(is\zeta) = -\frac{db_-}{d\zeta}\exp(-is\zeta). \qquad (3.7)$$

After substituting Eq.(3.5) into Eq.(3.4) and taking Eq.(3.6) into account, the system of solution can be expressed in the form [64]

$$\frac{d}{d\zeta}\begin{pmatrix} b_+ \\ b_- \end{pmatrix} = \frac{i\nu(\zeta)}{2s}\begin{pmatrix} -1 & -\exp(-2is\zeta) \\ \exp(2is\zeta) & 1 \end{pmatrix}\begin{pmatrix} b_+ \\ b_- \end{pmatrix}. \qquad (3.8)$$

where $\nu(\zeta) \equiv \omega_p'(\zeta)/c$. Consider the case that the reflectivity is small, $\mathbf{R} \ll 1$. The solution of system (3.8) corresponds to a known approximation in quantum mechanics with the potential considered as a perturbation [65]. By integrating the equation of $db_-/d\zeta$ from $\zeta = -\infty$ to ∞, we have

$$b_-(\infty) - b_-(-\infty) = \frac{i}{2s}\int_{-\infty}^{\infty} d\zeta\, \nu(\zeta)[b_+\exp(2is\zeta) + b_-]. \qquad (3.9)$$

Due to the small reflectivity, b_+ and b_- in the right hand side can be replaced by the zeroth order solution (a plane wave): $a^{(0)}(\zeta) = \exp(is\zeta)$, that is $b_+^{(0)} = 1$ and $b_-^{(0)} = 0$. This leads to

$$0 - \rho = \frac{i}{2s}\int_{-\infty}^{\infty} d\zeta\, \nu(\zeta)\exp(2is\zeta). \qquad (3.10)$$

After redefining the variable $\zeta = -\zeta$, the result is

$$\rho = \frac{i}{2s}\int_{-\infty}^{\infty} \nu(\zeta)\exp(-2is\zeta)d\zeta. \qquad (3.11)$$

Eq.(3.11) constructs the relation between the electron density profile ($\nu(\zeta)$) and the ratio between incident wave and reflected wave ρ.

On the other hand, the method utilized in [63] is shown as follows. Starting from the wave equation of the vector potential,

41

$$\left(\frac{\partial^2}{\partial x^2} - \frac{1}{c^2}\frac{\partial^2}{\partial t^2}\right)A'(x,t) = S'(x,t) = \frac{\omega_p'^{\,2}(x)}{c^2}A'(x,t), \qquad (3.12)$$

where A is the vector potential of the radiation, S is the source term and "'" is used to indicate quantities in the mirror's proper frame. The solution of A' can be written in the form

$$A'(x,t) = A'^{(0)} + \int\int dx'dt'\, G(x-x',t-t')S'(x',t'), \qquad (3.13)$$

where $A'^{(0)}$ is the zeroth order solution which corresponds to the solution of Eq.(3.12) without source, that is a planar wave. $G(x-x',t-t') = -(c/2)H[(t-t') - |x-x'|/c]$ is the Green's function of Eq.(3.12) that satisfies

$$\left(\frac{\partial^2}{\partial x^2} - \frac{1}{c^2}\frac{\partial^2}{\partial t^2}\right)G = \delta(x',t'). \qquad (3.14)$$

H is the Heaviside step function. The vector potential can be expressed in the iterative style

$$
\begin{aligned}
A'(x,t) &= A'^{(0)} + \int G\cdot\frac{\omega_p'^{\,2}}{c^2}\left(A'^{(0)} + \int G\cdot\frac{\omega_p'^{\,2}}{c^2}A'\right) \\
&= A'^{(0)} + \int G\cdot\frac{\omega_p'^{\,2}}{c^2}A'^{(0)} + \cdots \\
&\equiv A'^{(0)} + A'^{(1)} + \cdots
\end{aligned}
\qquad (3.15)
$$

If the contribution of the source term is small compared to the zeroth order term, that is when reflectivity is small, Eq.(3.15) is a perturbative equation to describe the vector potential. Here, we only keep terms up to the first order. Consider the zeroth order solution, a right-moving plane wave, to be $A^{(0)} = A_0\exp[i(\omega_s t - k_s x)]$ where A_0, ω_s and k_s are the amplitude, the angular frequency, and the wave number of incident wave, respectively.

42

The transmitted and reflected part of the incident wave can then be written as

$$A'_t \approx A'^{(0)} + A'^{(1)}(x \to +\infty, t), \tag{3.16}$$

$$A'_r \approx A'^{(1)}(x \to -\infty, t), \tag{3.17}$$

respectively. After substituting the Green's function into the first order term of Eq.(3.15), we have

$$A'^{(1)}(x,t) = -\frac{c}{2} \int_{-\infty}^{\infty} dx' \int_{-\infty}^{\infty} dt' H[(t - t') - |x - x'|/c] \frac{\omega_p'^2}{c^2} A'^{(0)}$$

$$= -\frac{c}{2} \int_{-\infty}^{\infty} dx' \int_{-\infty}^{t-|x-x'|/c} dt' \frac{\omega_p'^2}{c^2} A'^{(0)}, \tag{3.18}$$

where the property of the step function is used to arrive at the second equation. After carrying out the integration over t'

$$A'^{(1)}(x,t) = \frac{iA_0}{2k'_s} \int_{-\infty}^{\infty} dx' \frac{\omega_p'^2}{c^2} \exp[i(\omega'_s t - k'_s |x - x'| - k'_s x')], \tag{3.19}$$

where the relation $k'_s = \omega'_s/c$ is used. Consider the limit $(x \to -\infty)$ where $A'^{(1)} \approx A'_r$, $|x - x'| = x' - x$. After collecting terms, we have

$$A'_r(x,t) = \frac{iA_0}{2k'_s} \int_{-\infty}^{\infty} dx' \frac{\omega_p'^2}{c^2} e^{-2ik'_s x'} \times e^{i(\omega'_s t + k'_s x)} \tag{3.20}$$

$$\equiv A'_{r0} e^{i(\omega'_s t + k'_s x)}$$

It can be found that the reflected wave is left-moving as expected. The ratio of amplitude between reflected wave and incident wave is

$$\frac{A'_{r0}}{A_0} = \frac{i}{2k'_s} \int_{-\infty}^{\infty} dx' \frac{\omega_p'^2}{c^2} e^{-2ik'_s x'}. \tag{3.21}$$

It is noteworthy that the result is the same no matter using the method proposed by Bulanov et al. (Eq.(3.11)) or the one by H.-C, Wu (3.21) for calculating the reflection coefficient. After substituting the definition of ω_p and considering the ratio between amplitude of elec-

tric field, Eq.(3.21) can be expressed as

$$\frac{|E_r'(x,t)|}{|E_0|} = \frac{\mu_0 c e^2}{2 m_e \omega_s'} \int_{-\infty}^{\infty} dx' \, n'(x') e^{-2ik_s' x'}.$$
(3.22)

It is clear that the reflected electric field depends on the electron density distribution of the flying plasma mirror, $n(x)$. Here we discuss three different density distributions: Slab [63], Cusp [66], and Square-Root Lorentzian Distribution (SRLD), defined as

$$\text{Slab}: n_{slab}(x) = n_{peak}[H(x+2D) - H(x)],$$
(3.23)

$$\text{Cusp}: n_{cusp}(x) = 2^{1/3} n_0 \gamma \left(3x \frac{\omega_p}{\beta_{ph} c}\right)^{-2/3},$$
(3.24)

$$\text{SRLD}: n_{srld}(x) = n_{peak}\sqrt{\frac{L^2}{x^2 + L^2}},$$
(3.25)

where n_0 and n_{peak} are the unperturbed background plasma density and peak density of the distribution, separately. γ and β are the Lorentz factor and the normalized velocity, respectively, calculated from the phase velocity of the flying mirror. To compare the results from different density distributions, we unify the definition of mirror density in these three distributions. For Slab and SRLD, the peak density and thickness of the mirror can be associated with wave-breaking limit of the background plasma, under which the flying mirror contains half of the total electrons within the volume encompassed by the nonlinear plasma wavelength. Therefore, we have

$$\int_{-\lambda_{NP}/4}^{\lambda_{NP}/4} dx \, n_{slab}(x) = 2D n_{peak} = \frac{\lambda_{NP}}{2} n_0,$$
(3.26)

$$\int_{-\lambda_{NP}/4}^{\lambda_{NP}/4} dx \, n_{srld}(x) = 2L n_{peak} \sinh^{-1}(\lambda_{NP}/4L) = \frac{\lambda_N P}{2} n_0,$$
(3.27)

where λ_{NP} is the nonlinear plasma wavelength defined as $\lambda_{NP} \approx (2\sqrt{1 + a_0^2/2}/\pi)\lambda_p$ [39] (see also Sec.(2.3)), λ_p is the linear plasma wavelength and a_0 the normalized vector potential of a linearly polarized driver pulse. Then, we can link n_{peak} with background

density n_0, such as in SRLD case

$$n_{peak} = \frac{\lambda_{NP} n_0}{4L \sinh^{-1}(\lambda_{NP}/4L)}. \tag{3.28}$$

Besides, to make the comparison on an equal basis, we consider the same peak density of both Slab and SRLD distributions. The cusp distribution is with infinite peak density therefore can not be normalized in this way. With these considerations, Eq.(3.23)-(3.25) can be written as

$$\text{Slab}: \frac{n_{slab}(x)}{n_0} = \frac{C_{slab}}{D} \frac{c}{\omega_p}[H(x+2D) - H(x)], \tag{3.29}$$

$$\text{Cusp}: \frac{n_{cusp}(x)}{n_0} = 2^{1/3}\gamma\left(3x\frac{\omega_p}{\beta_{ph}c}\right)^{-2/3}, \tag{3.30}$$

$$\text{SRLD}: \frac{n_{srld}(x)}{n_0} = \frac{C_{srld}}{L} \frac{c}{\omega_p}\sqrt{\frac{L^2}{x^2+L^2}}, \tag{3.31}$$

where the normalization constants are defined as

$$C_{slab} \equiv \sqrt{1 + a_0^2/2}, \tag{3.32}$$

$$C_{srld} \equiv \frac{\sqrt{1 + a_0^2/2}}{\sinh^{-1}(\lambda_{NP}/4L)}. \tag{3.33}$$

The respective parameters used and suitable scene of these different distributions are explained as below. The Slab Distribution is a simplified model to describe the flying mirror with the thickness of the slab is defined as $2D$. This may be an approximated model in the interaction between intense laser and a solid target when all the electrons in the thin film are pushed away and formed a slab flying mirror. The Cusp Distribution is derived from the 1D cold, collisionless plasma theory and the nonlinear coupled wave equation at the wave breaking situation [60]. The SRLD is a fitting function that we deduced from the PIC simulation. From 1D PIC simulations, the peak density of the flying mirror was found to be not as spiky as the Cusp Distribution but more rounded instead. Actually, the singularity in the Cusp Distribution at the wave-breaking point may suggest the breakdown of the cold plasma description. For a typical Laser Wakefield Accelerator scheme, warm

45

plasma theory should take place as the flying mirror approaches the wave-breaking point, which in turn renders the maximum density finite [67]. Without solving the complex equations based on the warm plasma theory, we deduced the SRLD distribution as a good approximation to the flying mirror density near the wave-breaking limit (see the Inset of Fig.(3.1)). Here, L is the characteristic thickness of the flying mirror.

The reflectivity in terms of the photon number can be calculated from Eq.(3.22) by $\mathbf{R} \equiv |E'_r/E'_0|^2$. To transform the density function (Eq.(3.31)) into mirror's frame, it can be noted that the total electrons number in the distribution, N, is a Lorentz invariant. Thus, we have

$$\int_{-\infty}^{\infty} dx\, n(x) = \int_{-\infty}^{\infty} dx'\, n'(x') = N. \tag{3.34}$$

Here, we take the SRLD case as an example

$$\int_{-\infty}^{\infty} dx\, n_{peak} \sqrt{\frac{L^2}{x^2 + L^2}} = \int_{-\infty}^{\infty} \frac{dx'}{\gamma} n_{peak} \sqrt{\frac{L^2}{(x'/\gamma)^2 + L^2}}. \tag{3.35}$$

To arrive at the right hand side, the transformation $x' = \gamma x$ and $dx' = \gamma dx$ between mirror's frame and lab frame are used. Accordingly, the SRLD in mirror's frame is

$$n'(x') = \frac{n_{peak}}{\gamma} \sqrt{\frac{(\gamma L)^2}{(x')^2 + (\gamma L)^2}}. \tag{3.36}$$

The integration in Eq.(3.22) can then be carried out

$$\int_{-\infty}^{\infty} dx'\, n' e^{-2ik'_s x'} = 2n_{peak} L K_0(2\gamma L k'_s), \tag{3.37}$$

where K_0 is modified Bessel function of the second kind [68]. This gives the amplitude of the reflected wave for a SQLD mirror

$$\begin{aligned}
\frac{|E'_r(x,t)|}{|E'_0|} &= -\frac{\mu_0 c e^2}{2m_e \omega'_s} \times 2n_0 C_{srld} \frac{c}{\omega_p} K_0(2\gamma L k'_s) \\
&= \frac{\omega_p C_{srld}}{\omega'_s} K_0(2\gamma L k'_s).
\end{aligned} \tag{3.38}$$

46

The definition $\omega_p = n_0 e^2 / m_e \epsilon_0$ is used to simplified the equation. This leads to the reflection coefficient

$$\mathbf{R} \equiv \left|\frac{E_r'}{E_0'}\right|^2 = \left[\frac{\omega_p C_{srld}}{\omega_s'} K_0(2\gamma L k_s')\right]^2. \tag{3.39}$$
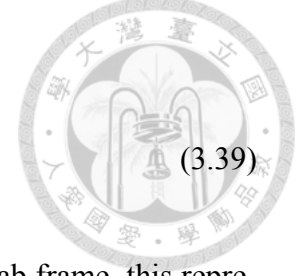
Note that this expression is calculated in the mirror's frame. In the lab frame, this represents the reflectivity in terms of number of photons (from here simply referred as "reflectivity").

The reflectivity for three different distributions are summarized as follows, parameters are all expressed with quantities in the lab frame [60, 63],

$$\text{Slab: } R_{slab}(\omega_s) = \left[\frac{\omega_p C_{slab}}{4\gamma\omega_s} \operatorname{sinc}(4\gamma^2\omega_s D/c)\right]^2, \tag{3.40}$$

$$\text{Cusp: } R_{cusp}(\omega_s) = \frac{\Gamma^2(2/3)}{2^2 \cdot 3^{4/3}} \left(\frac{\omega_p}{\omega_s}\right)^{8/3} \frac{1}{\gamma^{4/3}}, \tag{3.41}$$

$$\text{SRLD: } R_{srld}(\omega_s) = \left[\frac{\omega_p C_{srld}}{2\gamma\omega_s} K_0(4\gamma^2 L\omega_s/c)\right]^2, \tag{3.42}$$

where the sinc function is defined as $\operatorname{sinc}(x) \equiv \sin(x)/x$, Γ is the gamma function. From Eq.(3.40)-(3.42), it is clear that the reflectivity quickly decays as the frequency of incident wave ω_s increases. In addition, the reflectivity decreases as γ increases. This means that there exists a trade-off between high reflectivity and high frequency in the reflected wave.

The tendencies of such decrease in reflectivity are different among the three different density distributions of the sinc, the exponential ($\omega_s^{-8/3}$) and the K_0 functions, respectively. The decaying and oscillating behavior of the sinc function has been explained as the result of the modulations due to the constructive and destructive interferences [63]. It should be noted that the argument in the sinc function and K_0 are of the same form, defined as $s \equiv 4\gamma^2 L\omega_s/c = 2\pi L/\lambda_r$, where $\lambda_r \equiv 2\pi c/(4\gamma^2\omega_s)$ is the reflected wavelength in the lab frame. As $s \gg 1$, both sinc and K_0 functions decay quickly, which in turn highly suppress the reflectivity. Therefore, s can serve as a parameter to define the quality of the flying mirror. A good mirror is one whose thickness is roughly the same order of magnitude as the doubly Doppler shifted wavelength, i.e., $L \leq O(\lambda_r)$. This explains

47

why in an experiment one usually tunes the collision point at the wave-breaking limit so as to minimize the thickness of the flying mirror [49, 50], which is an optimum point for trade-off between the reflectivity and the frequency of the reflected wave.

To examine the validity of Eq.(3.40)-Eq.(3.42), we numerically study the property of relativistic flying mirror traversing a uniform plasma in the underdense regime with PIC simulations in 1D Cartesian geometry. The 1D configuration is a good approximation to the case of a driver pulse with a large focal spot in a higher dimension. This corresponds to the condition that $r \gg \lambda_p$ where r is the spot radius of the driver pulse and λ_p is the wavelength of the background plasma. The simulations are performed with the fully relativistic electromagnetic PIC code EPOCH [69].

In our simulation, the relativistic flying mirror is generated by a highly intense driver pulse (referred to as the "driver" from here on), which enters from the left boundary and propagates in the $+x$ direction. Along its way, the driver induces a flying mirror (wake-field) that follows behind it. The incident wave (referred to as the "source") enters, on the other hand, from the right boundary and propagates in the $-x$ direction. The collision point between the flying mirror and the source is tuned in such a way that the wave-breaking condition is reached with the flying mirror thickness minimized. Below we use subscripts "m","d","s" "r" to denote quantities that are associated with the flying mirror, the driver, the source and the reflected pulse, respectively.

The driver is characterized by the wavelength $\lambda_d = 800$nm and the normalized vector potential $a_d = 5.0$. The temporal profile is Gaussian with full-width-at-half-maximum (FWHM) duration of $\tau_d \approx \lambda_p/2$, which is chosen to excite the wakefield resonantly. The driver is linearly polarized with the electric field pointing in the y-direction.

To study the dependence of reflectivity on the source frequency, ω_s, several source wavelengths are chosen: 266nm, 400nm, 800nm, 1600nm, 2400nm and 4000nm. The normalized vector potential $a_s = 0.004$ is set to be small enough to prevent the recoil effect [55, 70]. The temporal profile is Gaussian with FWHM duration $\tau_s = 2T_s$, where $T_s = \lambda_s/c$ is the source cycle period. To distinguish the reflected pulse from the driver, we set the source linearly polarized in z-direction.

48

The background plasma density is uniform with a density $n_p = 0.025n_c$, where $n_c \equiv m_e \epsilon_0 \omega_d^2 / e^2$ is the critical plasma density with respect to the driver. The simulation box size is 80μm in the x direction with $160,000$ cells. For shorter λ_s, the finer the grid size so as to guarantee the spatial resolution is sufficient for tracking the blue-shifted reflected pulse. In our strictest case, the resolution of the Cartesian grid size is roughly 8.3 cells per reflected wavelength λ_r, which is estimated by $\lambda_r \approx \lambda_s/4\gamma_m^2$. Outflow conditions are applied to each simulation boundary for both electromagnetic waves and quasi-particles.
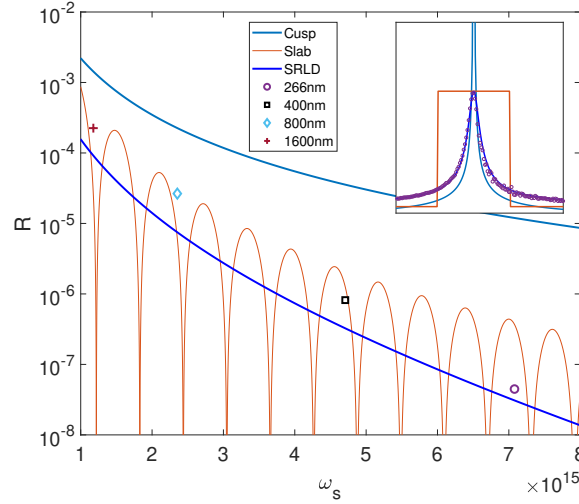

Figure 3.1: Reflectivity of the relativistic flying mirror as a function of the source frequency ω_s. Solid lines are calculated from different reflectivity models (Eq.(3.40)-(3.42)). Distinct symbols are PIC simulation results with different λ_s. SRLD model agrees well with PIC results and the cusp model approaches SRLD when a longer wavelength source is applied. Inset: Comparison between three density distribution (Eq.(3.29)-(3.31)) models and the density of flying mirror from PIC simulations. Note that the PIC data (circles) is almost overlapped by SRLD (blue line).

The comparison between the analytic formula and the simulation result on reflectivity is shown in Fig.(3.1). Parameters used in the analytic formulas (Eq.(3.40)-(3.42)) are $\omega_p = 3.72 \times 10^{14} \text{sec}^{-1}, a_d = 5, n_0 = 4.35 \times 10^{25} \text{m}^{-3}, \gamma = 4.08$ and $L = 1.12$nm. The first three parameters are fixed in the simulation setup while the last two are the values of the flying mirror at the collision point. The rightmost PIC data point is the one with the source wavelength $\lambda_s = 266$nm which corresponds to the frequency tripling of the frequency of the conventional 800nm Ti:Sapphire laser. In this setup, the double-Doppler-shifted wavelength $\lambda_r \approx 4$nm corresponds to the *water-window* X-ray wavelength, which can

49

be a useful tool for life science research. The reflectivity in terms of the photon number is $R \approx 5 \times 10^{-8}$, which is deduced from the ratio of the electric fields in the frequency spectrum between the reflected and the incident waves.

The reflectivity formula with the Cusp Distribution (Eq.(3.41)) may be a good estimation for long wavelength sources ($\lambda_s \geq \lambda_d$), such as the leftmost point in Fig.(3.1) or the case in [70] with $\lambda_s = 5\lambda_d$. However, as shown in Fig.(3.1), the discrepancy between Eq.(3.41) and the PIC result is found to grow as ω_s increases. With $\lambda_s = 266\text{nm}$ ($\lambda_s = \lambda_d/3$), we found that Eq.(3.41) tends to over-estimate the reflectivity by roughly two orders of magnitude. Within these three different models, the SRLD reflectivity formula gives the best agreement with the simulation results. This may not be surprising because one additional parameter, the thickness, was introduced in SRLD.

In the simulation, the resolution of the cell depends on the reflected wavelength λ_r. For a higher source frequency, a higher resolution is needed. However, with the help of Eq.(3.42), one can estimate the reflectivity directly from the property of the flying mirror. This helps to greatly accelerate the process to search for an appropriate experimental parameter space.

3.3 Frequency Deviation of the Reflected Spectrum

In the previous section, the incident wave was assumed to be a plane wave. In an actual experiment, however, the incident laser pulses are expected to have finite bandwidth. Here we consider such a pulse by a Gaussian wave packet with central frequency ω_s and pulse duration τ_s:

$$E_{in}(x,t) = E_0 e^{-t^2/\tau_s^2} e^{i(k_s x - \omega_s t)}. \tag{3.43}$$

To calculate the reflection of a finite-bandwidth pulse, we can use Fourier transform into the frequency space and discuss different frequency components separately. The electric

field amplitude in frequency space is

$$E_{in}(\omega) = \int dt \, E_{in}(x,t)e^{i\omega t} = E_0\tau_s\sqrt{\pi}\exp\left[\frac{-(\omega - \omega_s)^2}{4}\tau_s^2\right]. \qquad (3.44)$$

The transformation of $E_{in}(\omega)$ into mirror's proper frame can be realized by noting that the phase of electric field is a Lorentz invariant, that is $k_s x - \omega_s t = k_s' x' - \omega_s' t'$. The frequency in the co-moving frame is $\omega' = [(1 + \beta_m)/(1 - \beta_m)]^{1/2}\omega$. For simplifying the equation form, we consider the ultra-relativistic limit ($\beta \to 1$), this gives $\omega_s' = 2\gamma_m\omega_s$. Therefore we have the electric field amplitude in mirror's frame

$$E_{in}'(\omega') = E_0\tau_s\sqrt{\pi}\exp\left[\frac{-(\omega_s' - 2\gamma_m\omega_s)^2}{4}\left(\frac{\tau_s}{2\gamma_m}\right)^2\right]. \qquad (3.45)$$

It is clear that in this frame the central frequency of the wave packet is blue-shifted to $2\gamma_m\omega_s$ and the pulse duration shortened by the same factor $2\gamma_m$. The amplitude of the reflected wave can be calculated frequency by frequency

$$E_r'(\omega') = Y'(\omega') \cdot E_{in}'(\omega'), \qquad (3.46)$$

where $Y'(\omega')$ is the ratio between the amplitude of incident wave and reflected wave for a specific frequency ω' (cf. Eq.(3.22)). Accordingly, the electric field of the reflected wave from a flying mirror with a square-root Lorentzian distribution (Eq.(3.31)) in the mirror's proper frame can be calculated. After transforming back to the lab frame, the reflected electric field is

$$\left|\frac{E_r(\omega)}{E_0}\right| = 2\sqrt{\pi}\tau_s L\gamma_m C_{crld}\frac{\omega_p}{\omega}K_0(\frac{L\omega}{c}) \times \exp\left[\frac{-(\omega - 4\gamma_m^2\omega_s)^2}{4}\left(\frac{\tau_s}{4\gamma_m^2}\right)^2\right] \qquad (3.47)$$

It should be noted that, when the background plasma density is sufficiently low ($n_p/n_c \ll 1$), the parametric Doppler effect [60] due to the frequency dispersion in the background medium can be ignored. The exponential term describes a pulse with the central frequency at $4\gamma_m^2\omega_s$ and the pulse duration that is compressed by a factor $4\gamma_m^2$. However, the ω-dependent and decaying term, i.e., $K_0(L\omega/c)/\omega$, will distort the reflected

51

spectrum. Fig.(3.2) shows the normalized reflected spectrum with $\gamma_m = 5$, $L = 15$nm, and $\lambda_s = 800$nm. The red curve is the normalized exponential term. The blue curve is calculated from Eq.(3.47) and the black curve is the value of the decaying term. The distortion of the spectral shape, shown in the blue curve, is not evident, while both the frequency and the amplitude at the peak of the spectrum clearly deviate from the red curve.
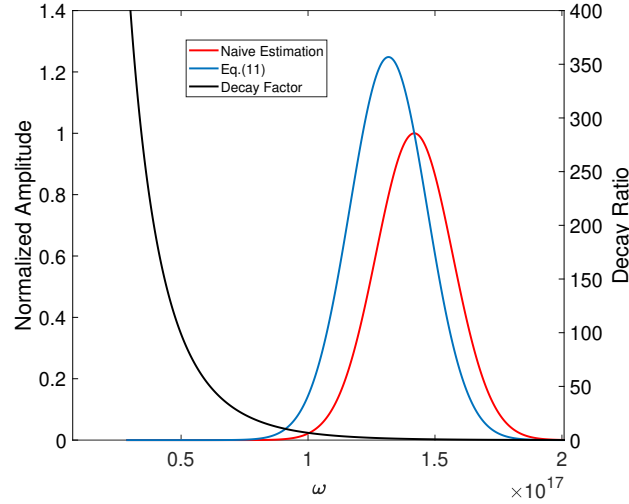

Figure 3.2: Normalized reflected electric field amplitude calculated by Eq.(3.47) (blue curve) and the naive estimation with $\omega = 4\gamma_m^2\omega_0$ (red curve). The black curve shows the decaying term in Eq.(3.47) and is also normalized to the value calculated with $\omega = 4\gamma_m^2\omega_0$. The deviation of both the frequency and amplitude at the peak of spectrum is demonstrated.

The deviation ratio between the frequency associated with the maximum amplitude, ω_{peak}, and the naively estimated frequency, $\omega_{est} \equiv 4\gamma_m^2\omega_s$, is defined as

$$\delta \equiv \frac{\omega_{peak} - \omega_{est}}{\omega_{est}} \tag{3.48}$$

From Eq.(3.47), δ depends mainly on three parameters: the pulse duration of source τ_s, the Lorentz factor of the flying mirror γ_m, and the characteristic thickness of the mirror L. Fig.(3.3) shows the dependence of δ on τ_s and γ_m, which are accessible in an experiment. τ_s can be measured with an auto-correlator and γ_m can be estimated by the background plasma density, $\gamma_m \approx \omega_0/\omega_p$ [26], or the energy of the accelerated electrons [50, 71].

The frequency associated with the maximum amplitude, ω_{peak}, can be calculated through $dE_r(\omega)/d\omega = 0$ at $\omega = \omega_{peak}$. However, due to the existence of the modified Bessel function of the second kind, ω_{peak} of Eq.(3.47) can not be found analytically. To have a

(a) Frequency Deviation Ratio and pulse duration

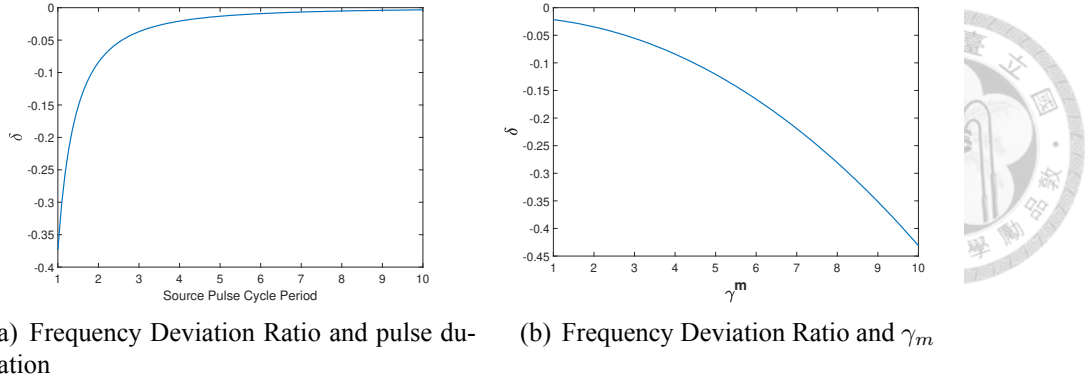(b) Frequency Deviation Ratio and γ_m

Figure 3.3: Dependence of δ on the pulse duration T and the Lorentz factor γ with other parameters fixed. The deviation is evident for few cycle source pulse or flying mirror with higher lorentz factor.

sense about the amount of deviation, we numerically solve the deviation with Eq.(3.47) based on the typical parameters of intense lasers: 30fs pulse duration and $\gamma_m = 4$. δ is found to be roughly -1%, which may be hard to detect. However, from Fig.(3.3), it can be seen that the deviation is more significant for fewer-cycle sources and flying mirrors with higher Lorentz factors. This implies that the correction cannot be neglected when few-cycle pulses are employed or high blue-shift reflections are demanded, such as the situation for generating attosecond pulses with relativistic flying mirrors [56].

To study the validity of Eq.(3.47), the code EPOCH [69] was used. Instead of flying mirrors induced by a driver laser, we imposed the mirror as an initial condition. The flying mirror was constructed as an electron sheet with a given longitudinal density distribution and propagating in the $+x$ direction with an initially assigned velocity. To prevent electrons from expelling each other during propagation, positive charge (proton) was introduced to co-move with the relativistic electron sheet. The interaction between protons and the source is negligible because of their large mass.

We used the simplified Square-Root Lorentzian Distribution, $n_m(x) = n_{m,0}\sqrt{L_m^2/(x^2 + L_m^2)}$, to characterize the density distribution of the flying mirror. There are three parameters to be determined: the peak density $n_{m,0}$, the characteristic thickness L_m, and the Lorentz factor of flying mirror γ_m. The peak density only affects the reflectivity. We therefore chose $n_{m,0} = 3n_c$, where n_c is the critical density for a 800nm electromagnetic wave, to guarantee that the reflected pulse is intense enough for observation. $\gamma_m = 4$ and L_m ranges

53

from 1nm to 20nm according to the PIC results from the laser-driven flying mirror. The source is a linearly polarized pulse with a wavelength $\lambda_s = 1.6\mu$m, which is long enough to increase the reflectivity. The normalized vector potential is $a_s = 0.004$. The temporal profile is Gaussian with FWHM duration $\tau_s = 1.5T_s$ where $T_s = \lambda_s/c$ is the source cycle period. The source enters from right boundary and propagates in $-x$ direction. The simulation box size is $50um$ in x direction with 25000 cells. Therefore, the resolution of the Cartesian grid is 12.5 cells per reflected wavelength, $\lambda_r \approx 4\gamma_m^2\lambda_s$. Boundary conditions remained the same as the setup in the previous section.
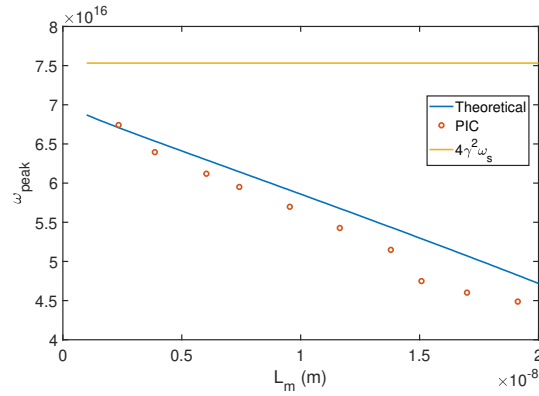

Figure 3.4: Comparison among the estimated double-Doppler shift frequency (yellow line), the theoretical prediction of ω_{peak} from Eq.(3.47) (blue line), and the PIC simulation result (red dots). $\gamma_m = 4$, $n_{m,0} = 3n_c$ and $\tau_s = 1.5T_s$ are used as the initial condition. The 1D PIC result agrees reasonably with theoretical prediction and the linear dependence of the deviation on mirror thickness is also illustrated.

The comparison between the theoretical prediction of the frequency at the peak amplitude from Eq.(3.47) and the PIC simulation results is shown in Fig.(3.4). The horizontal yellow line is the estimated naive frequency $4\gamma_m^2\omega_s$ and the blue one is the maximum value of Eq.(3.47) solved numerically. Red circles are the PIC simulation results with different characteristic thicknesses L_m. We see that the PIC results are in reasonable agreement with the theoretical prediction from Eq.(3.47). The discrepancy is resulted from the statistical fluctuations in the initialization of the SRLD distribution due to the limited number of macro-particles in our PIC simulations. From Fig.(3.4), the magnitude of the deviation, which is always negative, increases linearly as the characteristic thickness of the flying mirror L_m increases, where the slope depends on the Lorentz factor, γ_m, and the source pulse duration, τ_s.

54

In an actual experiment, γ_m can be deduced through the measurement of the reflected wave spectrum. Usually, this is estimated from the peak frequency of the reflected spectrum and the naive double-Doppler shifted relation, $\omega_{peak} = 4\gamma_m\omega_s$. The deviation from this idealized value, as we have shown, can serve as its correction that can further improve the precision of this method.

We have shown in Section II that the plasma mirror thickness is an important parameter that determines the reflectivity and the reflected spectrum. In actual experiments, multiple tools can be employed to diagnose the dynamics of the wakefield, i.e., the mirror, such as the relativistic electron bunch probe [72] and the optical probe [73]. However, the spatial and the temporal resolutions of these methods are still not precise enough to measure the thickness of a flying mirror near the wave-breaking condition, which is typically of tens of nanometer scale. Our investigation shows that the frequency deviation can serve as a diagnosis on the thickness. As Eq.(3.47) shows, the peak frequency of the reflected wave depends on ω_s, τ_s, γ_m, and L_m. Among them ω_s and τ_s are laser parameters that can be measured accurately. In principle, γ_m can be determined by conventional methods such as that based on the background plasma density [26] or the accelerated electron energy [50, 71], from which the mirror thickness can be deduced. However, the diagnostic scheme suggested here may require highly stable condition of lasers and plasmas.

3.4   Conclusion

In this section, we extended previous studies on the reflectivity of relativistic flying mirrors with incident plane waves. We showed that the Square Root Lorentzian Distribution can accurately describe the flying mirror density distribution, and can provide a better estimation about the reflectivity. We defined a dimensionless parameter, $s = 2\pi L_m/\lambda_r$, to characterize the quality of the flying mirror. To attain a high enough reflectivity, the condition, $s \leq 2\pi$, must be satisfied, which means that the mirror must be thinner than the wavelength of the reflected pulse. In our simulations, we demonstrated the feasibility of the generation of the water-window X-ray through plasma mirror reflection based on state-of-the-art laser parameters, which would provide great utility to life science re-

55

searches. We found that the reflectivity in this case is $\sim 5 \times 10^{-8}$ in photon numbers, which is encouraging. We also found that, for an incident wave with a Gaussian temporal profile, the peak frequency of the reflected spectrum is red-shifted from its expected value, $4\gamma_m^2 \omega_s$. The magnitude of the deviation is positively correlated to the thickness of the mirror and its Lorentz factor, but negatively correlated with the duration of the source pulse. This deviation helps to provide a better description of the reflected spectrum, which can serve as a diagnostic tool about the dynamics of the wakefield. These studies about the reflectivity and the reflected spectrum may benefit future experiments such as AnaBHEL.
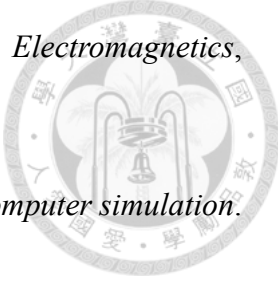
Bibliography

[1] Paul Gibbon. *Short pulse laser interactions with matter*. World Scientific Publishing Company Singapore, 2004.

[2] Stephen W Hawking. Black hole explosions? *Nature*, 248(5443):30–31, 1974.

[3] Stephen W Hawking. Breakdown of predictability in gravitational collapse. *Physical Review D*, 14(10):2460, 1976.

[4] Daniel Harlow. Jerusalem lectures on black holes and quantum information. *Reviews of Modern Physics*, 88(1):015002, 2016.

[5] William George Unruh. Experimental black-hole evaporation? *Physical Review Letters*, 46(21):1351, 1981.

[6] Oren Lahav, Amir Itah, Alex Blumkin, Carmit Gordon, Shahar Rinott, Alona Zayats, and Jeff Steinhauer. Realization of a sonic black hole analog in a bose-einstein condensate. *Physical review letters*, 105(24):240401, 2010.

[7] Jeff Steinhauer. Observation of self-amplifying hawking radiation in an analogue black-hole laser. *Nature Physics*, 10(11):864, 2014.

[8] Juan Ramón Muñoz de Nova, Katrine Golubkov, Victor I Kolobov, and Jeff Steinhauer. Observation of thermal hawking radiation and its temperature in an analogue black hole. *Nature*, 569(7758):688–691, 2019.

[9] PD Nation, MP Blencowe, AJ Rimberg, and E Buks. Analogue hawking radiation in a dc-squid array transmission line. *Physical review letters*, 103(8):087004, 2009.

[10] Bryce S DeWitt. Quantum field theory in curved spacetime. *Physics Reports*, 19(6):295–357, 1975.

[11] P.C.W. Davies and S.A. Fulling. Radiation from a moving mirror in two-dimensional space-time conformal anomaly. *Proc. Roy. Soc. Lond. A*, A348:393–414, 1976.

[12] N.D. Birrell and P.C.W. Davies. *Quantum Fields in Curved Space*. Cambridge Monographs on Mathematical Physics. Cambridge Univ. Press, Cambridge, UK, 1984.

[13] Frank Wilczek. Quantum purity at a small price: Easing a black hole paradox. *arXiv preprint hep-th/9302096*, 1993.

[14] Pisin Chen and Gerard Mourou. Accelerating Plasma Mirrors to Investigate Black Hole Information Loss Paradox. *Phys. Rev. Lett.*, 118(4):045001, 2017.

[15] Michael R.R. Good. *Quantized scalar fields under the influence of moving mirror and anisotropic curved spacetime*. PhD thesis, 2011.

[16] Stephen A Fulling and Paul CW Davies. Radiation from a moving mirror in two dimensional space-time: conformal anomaly. *Proceedings of the Royal Society of London. A. Mathematical and Physical Sciences*, 348(1654):393–414, 1976.

[17] SA Fulling. Review of some recent work on acceleration radiation. *Journal of Modern Optics*, 52(16):2207–2213, 2005.

[18] Robert D Carlitz and Raymond S Willey. Reflections on moving mirrors. *Physical Review D*, 36(8):2327, 1987.

[19] Pisin Chen and Dong-han Yeom. Entropy evolution of moving mirrors and the information loss problem. *Physical Review D*, 96(2):025016, 2017.

[20] Pisin Chen and Gerard Mourou. Accelerating plasma mirrors to investigate the black hole information loss paradox. *Physical review letters*, 118(4):045001, 2017.

[21] Pisin Chen. Trajectory of a flying plasma mirror traversing a target with density gradient. *arXiv preprint arXiv:2004.10615*, 2020.

[22] Irving Langmuir. Oscillations in ionized gases. *Proceedings of the National Academy of Sciences of the United States of America*, 14(8):627, 1928.

[23] Francis F Chen et al. *Introduction to plasma physics and controlled fusion*, volume 1. Springer, 1984.

[24] Theodore H Maiman. Stimulated optical radiation in ruby. *nature*, 187(4736):493–494, 1960.

[25] Donna Strickland and Gerard Mourou. Compression of amplified chirped optical pulses. *Optics communications*, 56(3):219–221, 1985.

[26] Toshiki Tajima and John M Dawson. Laser electron accelerator. *Physical Review Letters*, 43(4):267, 1979.

[27] Victor Malka, S Fritzler, E Lefebvre, M-M Aleonard, F Burgy, J-P Chambaret, J-F Chemin, K Krushelnick, G Malka, SPD Mangles, et al. Electron acceleration by a wake field forced by an intense ultrashort laser pulse. *Science*, 298(5598):1596–1600, 2002.

[28] Gerard Mourou and Toshiki Tajima. More intense, shorter pulses. *Science*, 331(6013):41–42, 2011.

[29] Gerard A Mourou, Toshiki Tajima, and Sergei V Bulanov. Optics in the relativistic regime. *Reviews of modern physics*, 78(2):309, 2006.

[30] John M Dawson. Particle simulation of plasmas. *Reviews of modern physics*, 55(2):403, 1983.

[31] Kane Yee. Numerical solution of initial boundary value problems involving maxwell's equations in isotropic media. *IEEE Transactions on antennas and propagation*, 14(3):302–307, 1966.
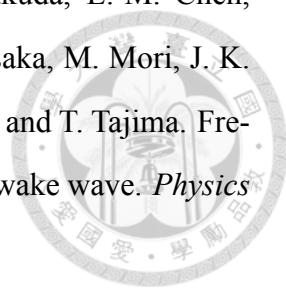
[32] Stephen D Gedney. Introduction to the finite-difference time-domain (fdtd) method for electromagnetics. *Synthesis Lectures on Computational Electromagnetics*, 6(1):1–250, 2011.

[33] Charles K Birdsall and A Bruce Langdon. *Plasma physics via computer simulation*. CRC press, 2004.

[34] William H Press, Brian P Flannery, Saul A Teukolsky, William T Vetterling, et al. *Numerical recipes*, volume 3. Cambridge University Press Cambridge, 1989.

[35] Aleksander Ilyich Akhiezer and RV Polovin. Theory of wave motion of an electron plasma. *Soviet Phys. JETP*, 3, 1956.

[36] SV Bulanov, VI Kirsanov, and AS Sakharov. Excitation of ultrarelativistic plasma waves by pulse of electromagnetic radiation. *JETP Lett*, 50(4):198–201, 1989.

[37] P Sprangle, E Esarey, and A Ting. Nonlinear interaction of intense laser pulses in plasmas. *Physical review A*, 41(8):4463, 1990.

[38] P Sprangle, E Esarey, and A Ting. Nonlinear theory of intense laser-plasma interactions. *Physical review letters*, 64(17):2011, 1990.

[39] V.I. Berezhiani and I.G. Murusidze. Relativistic wake-field generation by an intense laser pulse in a plasma. *Physics Letters A*, 148(6):338 – 340, 1990.

[40] Pisin Chen, J. M. Dawson, Robert W. Huff, and T. Katsouleas. Acceleration of electrons by the interaction of a bunched electron beam with a plasma. *Phys. Rev. Lett.*, 54:693–696, Feb 1985.

[41] Sergei Bulanov, Nataria Naumova, Francesco Pegoraro, and Junichi Sakai. Particle injection into the wave acceleration phase due to nonlinear wake wave breaking. *Physical Review E*, 58(5):R5257, 1998.

[42] AJ Gonsalves, Kei Nakamura, Chen Lin, Dmitriy Panasenko, Satomi Shiraishi, Thomas Sokollik, Carlo Benedetti, CB Schroeder, CGR Geddes, Jeroen Van Tilborg,

et al. Tunable laser plasma accelerator based on longitudinal density tailoring. *Nature Physics*, 7(11):862–866, 2011.
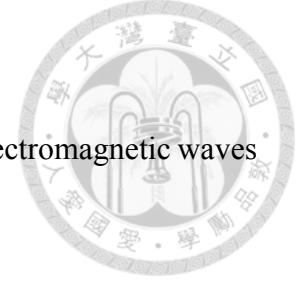
[43] CD Decker and WB Mori. Group velocity of large amplitude electromagnetic waves in a plasma. *Physical review letters*, 72(4):490, 1994.

[44] E Esarey, CB Schroeder, BA Shadwick, JS Wurtele, and WP Leemans. Nonlinear theory of nonparaxial laser pulse propagation in plasma channels. *Physical review letters*, 84(14):3081, 2000.

[45] Carl B Schroeder, Carlo Benedetti, Eric Esarey, and WP Leemans. Nonlinear pulse propagation and phase velocity of laser-driven plasma waves. *Physical review letters*, 106(13):135002, 2011.

[46] Mathieu Lobet, Masaki Kando, James K Koga, Timur Zh Esirkepov, Tatsufumi Nakamura, Alexander S Pirozhkov, and Sergei V Bulanov. Controlling the generation of high frequency electromagnetic pulses with relativistic flying mirrors using an inhomogeneous plasma. *Physics Letters A*, 377(15):1114–1118, 2013.

[47] A. Einstein. Zur elektrodynamik bewegter körper. *Annalen der Physik*, 322(10):891–921, 1905.

[48] Sergei V. Bulanov, Timur Esirkepov, and Toshiki Tajima. Light intensification towards the schwinger limit. *Phys. Rev. Lett.*, 91:085001, Aug 2003.

[49] M. Kando et al. Demonstration of laser-frequency upshift by electron-density modulations in a plasma wakefield. *Phys. Rev. Lett.*, 99:135001, 2007.

[50] Masaki Kando, A Pirozhkov, Keigo Kawase, T Esirkepov, Yuji Fukuda, Hiromitsu Kiriyama, Hidechika Okada, Daito Izuru, T Kameshima, Yoshiki Hayashi, H Kotaki, M Mori, J Koga, H Daido, A.Ya Faenov, Tatiana Pikuz, J. Ma, Li Chen, Evgenii Ragozin, and S Bulanov. Enhancement of photon number reflected by the relativistic flying mirror. *Physical review letters*, 103:235003, 12 2009.

[51] A. S. Pirozhkov, J. Ma, M. Kando, T. Zh. Esirkepov, Y. Fukuda, L.-M. Chen, I. Daito, K. Ogura, T. Homma, Y. Hayashi, H. Kotaki, A. Sagisaka, M. Mori, J. K. Koga, T. Kawachi, H. Daido, S. V. Bulanov, T. Kimura, Y. Kato, and T. Tajima. Frequency multiplication of light back-reflected from a relativistic wake wave. *Physics of Plasmas*, 14(12):123106, 2007.

[52] W. J. Ma, J. H. Bin, H. Y. Wang, M. Yeung, C. Kreuzer, M. Streeter, P. S. Foster, S. Cousens, D. Kiefer, B. Dromey, X. Q. Yan, J. Meyer-ter Vehn, M. Zepf, and J. Schreiber. Bright subcycle extreme ultraviolet bursts from a single dense relativistic electron sheet. *Phys. Rev. Lett.*, 113:235002, Dec 2014.

[53] Henri Vincenti. Achieving extreme light intensities using optically curved relativistic plasma mirrors. *Phys. Rev. Lett.*, 123:105001, Sep 2019.

[54] Alexander S. Pirozhkov, Sergei V. Bulanov, Timur Zh. Esirkepov, Michiaki Mori, Akito Sagisaka, and Hiroyuki Daido. Attosecond pulse generation in the relativistic regime of the laser-foil interaction: The sliding mirror model. *Physics of Plasmas*, 13(1):013107, 2006.

[55] James K Koga, Sergei V Bulanov, Timur Zh Esirkepov, Masaki Kando, Stepan S Bulanov, and Alexander S Pirozhkov. Relativisitcally upshifted higher harmonic generation via relativistic flying mirrors. *Plasma Physics and Controlled Fusion*, 60(7):074007, may 2018.

[56] Hoda Moghadasin, Ali Reza Niknam, Davood Komaizi, and Mohammadreza Banjafar. Attosecond pulse generation by relativistic flying mirrors in laser-plasma interaction: Effect of plasma density and driver amplitude on the generated pulse. *Physics of Plasmas*, 26(9):093105, 2019.

[57] J. Mu, T. Zh. Esirkepov, P. Valenta, T. M. Jeong, Ya. Gu, J. K. Koga, A. S. Pirozhkov, M. Kando, G. Korn, and S. V. Bulanov. High-order harmonics from laser irradiated electron density singularity formed at the bow wave in the laser plasma. *Physics of Wave Phenomena*, 27(4):247–256, Oct 2019.

[58] P. C. W. Davies and S. A. Fulling. Radiation from moving mirrors and from black holes. *Proceedings of the Royal Society of London. Series A, Mathematical and Physical Sciences*, 356(1685):237–257, 1977.

[59] Pisin Chen. Trajectory of a flying plasma mirror traversing a target with density gradient. *arXiv preprint arXiv:2004.10615*, 2020.

[60] S. V. Bulanov, T. Zh Esirkepov, M. Kando, A. S. Pirozhkov, and N. N. Rosanov. Relativistic mirrors in plasmas. Novel results and perspectives. *Physics Uspekhi*, 56(5):429–464, May 2013.

[61] K.N. Lin, C.E. Chou, and P. Chen. Particle production by a relativistic semi-transparent mirror in 1+3d minkowski spacetime. (Manuscript in preparation, 2020).

[62] C.E. Chou, K.N. Lin, and P. Chen. Partially reflective dynamical casimir effect with a relativistic mirror. (Manuscript in preparation, 2020).

[63] H-C Wu and Jürgen Meyer-ter Vehn. The reflectivity of relativistic ultra-thin electron layers. *The European Physical Journal D*, 55(2):443–449, 2009.

[64] Michael V Berry. Semiclassically weak reflections above analytic and non-analytic potential barriers. *Journal of Physics A: Mathematical and General*, 15(12):3693, 1982.

[65] Lev Davidovich Landau and Evgenii Mikhailovich Lifshitz. *Quantum mechanics: non-relativistic theory*, volume 3. Elsevier, 2013.

[66] SV Bulanov, Francesco Califano, GI Dudnikova, T Zh Esirkepov, IN Inovenkov, FF Kamenets, TV Liseikina, M Lontano, K Mima, NM Naumova, et al. Relativistic interaction of laser pulses with plasmas. In *Reviews of Plasma Physics*, pages 227–335. Springer, 2001.

[67] C Schroeder, E Esarey, and BA Shadwick. Warm wave breaking of nonlinear plasma waves with arbitrary phase velocities. *Physical review. E, Statistical, nonlinear, and soft matter physics*, 72:055401, 12 2005.

[68] Milton Abramowitz. *Handbook of Mathematical Functions, With Formulas, Graphs, and Mathematical Tables,*. Dover Publications, Inc., USA, 1974.

[69] T D Arber, K Bennett, C S Brady, A Lawrence-Douglas, M G Ramsay, N J Sircombe, P Gillies, R G Evans, H Schmitz, A R Bell, and C P Ridgers. Contemporary particle-in-cell approach to laser-plasma modelling. *Plasma Physics and Controlled Fusion*, 57(11):113001, sep 2015.

[70] P. Valenta, T. Zh. Esirkepov, J. K. Koga, A. S. Pirozhkov, M. Kando, T. Kawachi, Y.-K. Liu, P. Fang, P. Chen, J. Mu, G. Korn, O. Klimo, and S. V. Bulanov. Recoil effects on reflection from relativistic mirrors in laser plasmas. *Physics of Plasmas*, 27(3):032109, 2020.

[71] Eric Esarey and Mark Pilloff. Trapping and acceleration in nonlinear plasma waves. *Physics of Plasmas*, 2(5):1432–1436, 1995.

[72] C. J. Zhang, J. F. Hua, Y. Wan, C.-H. Pai, B. Guo, J. Zhang, Y. Ma, F. Li, Y. P. Wu, H.-H. Chu, Y. Q. Gu, X. L. Xu, W. B. Mori, C. Joshi, J. Wang, and W. Lu. Femtosecond probing of plasma wakefields and observation of the plasma wake reversal using a relativistic electron bunch. *Phys. Rev. Lett.*, 119:064801, Aug 2017.

[73] M. B. Schwab, A. Sävert, O. Jäckel, J. Polz, M. Schnell, T. Rinck, L. Veisz, M. Möller, P. Hansinger, G. G. Paulus, and M. C. Kaluza. Few-cycle optical probe-pulse for investigation of relativistic laser-plasma interactions. *Applied Physics Letters*, 103(19):191118, 2013.